Upper ocean heat and salt balances in response to a westerly wind burst in the western equatorial Pacific during TOGA COARE

Ming Feng,[1] Peter Hacker, and Roger Lukas

School of Ocean and Earth Science and Technology, University of Hawaii, Honolulu

Abstract. Two volume control methods are used to analyze the upper ocean heat and salt balances in response to a westerly wind burst event in the western equatorial Pacific during the Tropical Ocean Global Atmosphere Coupled Ocean-Atmosphere Response Experiment. One method uses a fixed-thickness surface layer, and the other uses an isopycnal depth as the lower boundary. Horizontal advection terms in the budget calculations are estimated using the R/V *Wecoma* repeat hydrographic survey data within a 133 km × 133 km region. In both methods, the upper ocean heat budget is balanced within 10 W m^{-2} of the surface air-sea flux observations during a 19-day time period, which covers the December 1992 westerly wind burst and a low-wind recovery period in early January 1993. The standard error in the estimation of heat advection is 11 W m^{-2}. The salt budget yields a rain rate estimate of 15.4 mm d^{-1} with an error bar of 4 mm d^{-1}. This estimate is within 20% of the optical rain gauge measurements. The advection terms are important in both the heat and salt balances. Meridional advection dominates over zonal and vertical advection, acting to decrease temperature and increase salinity in the surface layer. From the isopycnal boundary method, the diapycnal turbulent flux transports a mean heat flux of 17 W m^{-2} into the thermocline. Diapycnal advection is almost equally important, so that the total heat flux into the thermocline is estimated to be more than 30 W m^{-2} during the study time period. Both terms are also important in the salt budget.

1. Introduction

The western equatorial Pacific warm pool, where sea surface temperature exceeds 29°C, is the warmest open ocean water in the world. It plays an important role in the ocean-atmosphere coupling during the El Nino Southern Oscillation events [*Webster and Lukas*, 1992]. Extensive upper ocean and air-sea flux observations were conducted in the intensive flux array (IFA) centered at 2° S, 156° E in the warm pool during the Tropical Ocean Global Atmosphere (TOGA) Coupled Ocean-Atmosphere Response Experiment (COARE) intensive observing period (IOP) from November 1992 through February 1993. The goal of these observations was to quantify the air-sea interaction processes, especially those associated with the westerly wind burst (WWB) phenomenon in the warm pool region [*Webster and Lukas*, 1992].

During the IOP, strong intraseasonal oscillations (ISO) occurred within the IFA. The ISO, or 30-60 oscillation, is characterized by an eastward propagation of a large-scale region of anomalous deep convection [*Chen et al.*, 1996]. The anomalous convection shows multiscale structures in time and space. The active phase of the ISO is associated with intermittent, strong surface westerly wind anomalies known as WWBs, which typically last for less than 1 week [*Weller and Anderson*, 1996; *Harrison and Vecchi*, 1997]. The WWB has a meridional scale of a few hundred kilometers and a zonal scale of more than 1000 km, can generate strong equatorial waves, and can strongly affect the air-sea interaction processes in the tropics.

This paper utilizes the IOP observations to address two issues; one is to determine the important oceanic processes that affect the upper ocean heat and salt balances in response to a WWB during December 1992 to early January 1993, and the other is to use the heat and salt balances in the upper ocean to evaluate the independent estimates of heat and freshwater fluxes across the air-sea interface.

It has been difficult to improve closure of the surface energy budget in the warm pool to better than 60-80 W m^{-2} before COARE observations [*Godfrey and*

[1] Also at Institute of Oceanology, Chinese Academy of Sciences, Qingdao, People's Republic of China.

Lindstrom, 1989]. The freshwater budget in this region is also a challenge due to the large net freshwater flux [*Donguy*, 1987; *Lukas and Lindstrom*, 1991]. Using COARE bulk formulae [*Fairall et al.*, 1996], *Weller and Anderson* [1996] calculate the flux terms using surface meteorology observations from a central mooring (deployed by Woods Hole Oceanographic Institute, hereafter called the WHOI mooring). On the basis of intercomparisons with nearby ships, they find that the uncertainty in the net heat flux can be reduced to less than 10 Wm^{-2} in means computed over one to several weeks. However, there are still discrepancies in the mean rain rate estimates from different platforms [*Godfrey et al.*, 1997].

Previous upper ocean budget studies for the IOP suggested that one-dimensional (1-D) physics sometimes is not enough to describe the upper ocean responses to a WWB [*Smyth et al.*, 1996b; *Anderson et al.*, 1996; *Cronin and McPhaden*, 1997]. Calculations of the 3-D heat and salt budgets at the center of the IFA are the subjects of this paper and a paper by Antonissen et al. (personal communication, 1997).

During the IOP, the research vessel (R/V) *Wecoma* conducted a repeated butterfly pattern survey centered at 1.8° S, 156.1° E with a spatial extent of 133 km in both zonal and meridional directions (Figure 1). Each circuit of the butterfly took about 1.5 days. Temperature, salinity, and velocity profiles were measured along the track [*Huyer et al.*, 1997]. In this paper, two volume control methods are used to analyze the 3-D upper ocean heat and salt budgets from the R/V *Wecoma* data over the butterfly survey domain. One is a fixed thickness surface layer analysis, and the other uses an isopycnal depth to bound the volume [*Stevenson and*
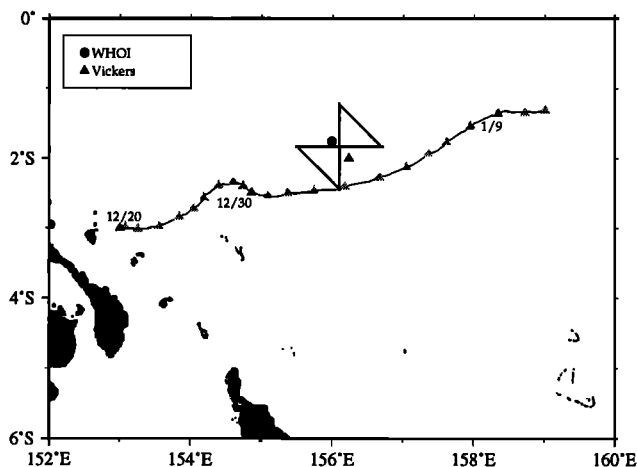
Figure 1. Intensive flux array region map. Solid areas are islands. The bold line is the standard butterfly pattern of the R/V *Wecoma*. The circle is the position of the WHOI buoy and the R/V *Moana Wave*, and the solid triangle is the position of the R/V *Vickers*. The light line is the time integration of the 5-m WHOI current from December 20, 1992, to January 10, 1993. The spacing between the shaded triangles is 1 day.

Niiler, 1983; *Cronin and McPhaden*, 1997; Godfrey et al., personal communication, 1996]. The fixed-thickness method is easy to develop, and we can recognize which advection terms play important roles in the budget. However, this method is very sensitive to the vertical motion of the thermocline. The benefit of the isopycnal boundary method is that we can more closely relate the mean temperature in the layer to the sea surface temperature [*Stevenson and Niiler*, 1983], and we can eliminate the vertical advection effects of low-mode internal waves.

This paper is organized as follows: in section 2, we introduce the data sets used in the present study; in section 3, we introduce the formulae for the heat and salt budgets in the two volume control methods and the calculation methods for different terms; in section 4, we give the calculation results; and in section 5, we discuss the results, followed by a short summary in section 6.

2. Data

Figure 1 gives the positions of the IOP observations. The WHOI mooring was located at 1°45'S, 156° E at a water depth of 1744 m, the R/V *Moana Wave* was within 10 km of the WHOI mooring, and the R/V *Vickers* was at 2° S, 156.2° E, all near the center of the R/V *Wecoma* butterfly survey.

The WHOI mooring provided continuous meteorological and oceanographic measurements for the duration of the IOP. Sensors on its surface buoy sampled wind speed and direction, relative humidity, air temperature, barometric pressure, incoming shortwave radiation, incoming longwave radiation, sea surface temperature, and current speed and direction at 5 m depth [*Weller and Anderson*, 1996]. The COARE version 2.5 bulk formulae [*Fairall et al.*, 1996] have been used to calculate the latent and sensible heat fluxes, and true sea surface temperature or skin temperature was used to estimate the outgoing radiation [*Weller and Anderson*, 1996]. We have applied a 7 Wm^{-2} decrease of the net longwave radiation as suggested by *Bradley and Weller* [1997]. The rain rate data are from the optical rain gauge measurements on the *R/V Moana Wave*; also, the sensible heat flux due to rainfall has been calculated from the R/V *Moana Wave* measurements by *Fairall et al.* [1996]. The flux data used herein are hourly averages.

The R/V *Wecoma* observations were made on three cruises. We use the cruise 2 data for the present study (during December 20, 1992, to January 8, 1993 [*Huyer et al.*, 1997]). Continuous acoustic Doppler current profiler velocity measurements were made from 18 to about 300 m. For our analysis, we use gridded data vertically averaged to 10-m-depth bins. The Seasoar conductivity-temperature-depth temperature and salinity measurements were gridded from the surface to about 250 dbar with a 2 dbar spacing. The horizontal resolution is about 1.5 km, with data gaps near

the surface and 250 dbar on some sections because of variable Seasoar handling. For our analysis, the velocity, temperature, salinity and potential density data are averaged hourly. Only the data that fall in the butterfly region are used. The Seasoar data are accurate to $\pm 0.01°C$ in temperature, ± 0.01 practical salinity unit (psu) in salinity, and ± 1 dbar in pressure [*Huyer et al.*, 1997]. The hourly velocity data have an accuracy of ± 1 cm s^{-1}.

Additionally, microstructure measurements were made from the CHAMELEON profiler [*Moum et al.*, 1995] on the R/V *Moana Wave*. Temperature, salinity, potential density, Brunt-Vaisala frequency, and turbulent kinetic energy dissipation rate (ϵ) profiles have been computed using these data. The vertical resolution is 4 m. The hourly mean data were calculated by *Smyth et al.* [1996a]. Also, solar radiation penetration profiles have been daily averaged for the R/V *Vickers* measurements [*Siegel et al.*, 1995]. These data are for every meter from 1 to 100 m.

3. Methods

In this section, we first introduce the formulae for the heat and salt budgets of the two volume control methods. Then we give the calculation methods for different terms.

3.1. Fixed Thickness Method

Assuming no horizontal mixing, the temperature and salinity tendency equations are written as

$$\rho_0 c_p \left(\frac{\partial T}{\partial t} + \mathbf{u} \cdot \nabla T + w \frac{\partial T}{\partial z} \right) = \frac{\partial R_S}{\partial z} - \frac{\partial F_T}{\partial z}, \quad (1)$$

$$\frac{\partial S}{\partial t} + \mathbf{u} \cdot \nabla S + w \frac{\partial S}{\partial z} = -\frac{\partial F_S}{\partial z}. \quad (2)$$

The variable ρ_0 is the mean water density, c_p is the specific heat, $\mathbf{u} = (u, v)$ is the horizontal velocity, w is the vertical velocity, R_S is the penetrating solar radiation, and F_T and F_S are the vertical turbulent heat and salt fluxes, respectively.

Vertically integrating the above heat and salt tendency equations from a fixed depth h to the sea surface, the following forms are obtained:

$$\int_{-h}^{0} \rho_0 c_p \frac{\partial T}{\partial t} dz = -\int_{-h}^{0} \rho_0 c_p \left(\mathbf{u} \cdot \nabla T + w \frac{\partial T}{\partial z} \right) dz$$
$$- Q_0 + R_S|_{-h} + F_T|_{-h}, \quad (3)$$

$$\int_{-h}^{0} \frac{\partial S}{\partial t} dz = -\int_{-h}^{0} \left(\mathbf{u} \cdot \nabla S + w \frac{\partial S}{\partial z} \right) dz$$
$$- S_0(P - E) + F_S|_{-h}. \quad (4)$$

$Q_0 = R_S(0) + F_T(0)$ is the net surface heat flux, $R_S|_{-h}$ is the penetrating solar radiation at h, S_0 is the surface salinity, P and E are the precipitation and evaporation rates, respectively, and $F_T|_{-h}$ and $F_S|_{-h}$ are the turbulent heat and salt fluxes at h, respectively.

3.2. Isopycnal Boundary Method

The isopycnal selected for this purpose has a depth h just below the mixed layer during the WWB, so that it can best represent the active surface layer and minimize the influence of variations in the thermocline. The equations (1) and (2) are rewritten in the sense of vertical mean temperature and salinity over the layer between the sea surface and the isopycnal depth following *Stevenson and Niiler* [1983]. In this format, the adiabatic variations due to the vertical displacements of the thermocline are excluded from the calculation, and it is easy to integrate with time. The rewritten equations are

$$\frac{\partial \overline{T}}{\partial t} = \frac{1}{\rho c_p h} \left(-Q_0 + R_S|_{-h} + F_T|_{-h} \right) - \frac{\overline{T} - T_{-h}}{h} w_e$$
$$- \overline{\mathbf{u}} \cdot \nabla \overline{T} - \frac{1}{h} \nabla \cdot \int_{-h}^{0} T' \mathbf{u}' dz, \quad (5)$$

$$\frac{\partial \overline{S}}{\partial t} = \frac{1}{h} \left((-S_0(P - E) + F_S|_{-h}) - \frac{\overline{S} - S_{-h}}{h} w_e \right.$$
$$- \overline{\mathbf{u}} \cdot \nabla \overline{S} - \frac{1}{h} \nabla \cdot \int_{-h}^{0} S' \mathbf{u}' dz, \quad (6)$$

where $\overline{T} = \frac{1}{h} \int_{-h}^{0} T dz$, $T' = T - \overline{T}$, $\overline{S} = \frac{1}{h} \int_{-h}^{0} S dz$, $S' = S - \overline{S}$, and $\overline{\mathbf{u}} = \frac{1}{h} \int_{-h}^{0} \mathbf{u} dz$, and $\mathbf{u}' = \mathbf{u} - \overline{\mathbf{u}}$. $\overline{T}$, $\overline{S}$, and $\overline{\mathbf{u}}$ are the mean temperature, salinity, and horizontal velocity, respectively; T', S', and $\mathbf{u}'$ are the deviations from the vertical mean values in the water column; Q_0, R_S, F_T, S_0, P, E, and F_S are the same as in the fixed depth analysis; $T|_{-h}$, $S|_{-h}$ and $w|_{-h}$ are the temperature, salinity, and vertical velocity at h, respectively. Note that h is a function of time and horizontal space. The value $w_e = dh/dt + w|_{-h}$ is the diapycnal velocity, where $d/dt = \partial/\partial t + u\partial/\partial x + v\partial/\partial y$.

The last two terms in (5) and (6) are the horizontal advection terms. The first term is the vertical mean horizontal velocity acting on the horizontal gradients of vertical mean temperature (salinity), and the second term is the convergence of heat (salt) due to a stratified shear flow. Some authors have neglected the second advection term, because they do not have credible measurements to estimate this term [*Stevenson and Niiler*, 1983; *Cronin and McPhaden*, 1997]. In this study, we estimate both terms based on the R/V *Wecoma* data.

3.3. Evaluation of Different Terms

3.3.1. Temporal and spatial gradients.
In the two volume control methods, it is necessary to estimate

the mean values and the temporal and spatial gradients of the variables such as T, S, ρ, and u in a certain layer and $\overline{T}$, $\overline{S}$, $\overline{u}$, h, $\int_{-h}^{0} T'u'dz$, and $\int_{-h}^{0} S'u'dz$, etc. On the basis of the R/V *Wecoma* survey pattern, the above variables over two complete butterfly circuits (approximately 3 days) are fit with a mean value and linear trends in time and horizontal space. Note that the approximately 3-day fit period represents a compromise: short enough so that near-inertial period changes can be resolved and long enough to obtain two measurements in time at each spatial location for evaluation of the temporal tendency and to suppress the tidal noise. Thus we evaluate

$$d(x(t), y(t), t) = \overline{d} + d_x x + d_y y + d_t t$$
$$+ d'(x(t), y(t), t). \qquad (7)$$

Variable $d = d(x(t), y(t), t)$ is the variable to be fit, x and y are the longitude and latitude, respectively, relative to the crossover point, t is the time relative to the center time of the interval, $\overline{d}$, d_x, d_y, and d_t are constants, and d' is the residual. In this sense, the $\overline{d}$ represents the mean value of d at the crossover point, d_x and d_y represent the mean zonal and meridional gradients, and d_t is mean rate of temporal change. The vertical gradients of T and S in the vertical advection term are calculated as the vertical gradients of $\overline{T}$ and $\overline{S}$. Moving the near 3-day window forward, the time series of all variables are obtained. Bootstrap analysis [*Efron and Tibshirani*, 1986] is used to estimate the errors in the mean value and gradients (Appendix A). Considering a peak velocity of 50 cm s^{-1} in the surface layer during WWB, the advection distance is about 65 km (smaller than the survey domain) in 1.5 days. Thus we can evaluate the advection effects for both heat and salt balances from the R/V *Wecoma* data.

3.3.2. Turbulent fluxes. The turbulent heat and salt fluxes at a certain depth are calculated as

$$F_T = -\rho c_p K_T \frac{\partial T}{\partial z} \qquad F_S = -K_S \frac{\partial S}{\partial z}, \qquad (8)$$

where the thermal and haline diffusivities are set equal to the density diffusivity, $K_T = K_S = K_\rho = \Gamma \epsilon / N^2$. The variable ϵ is the turbulent kinetic energy dissipation rate calculated from the microstructure measurements [*Smyth et al.*, 1996b]. N is the buoyancy frequency, and Γ is the mixing efficiency [*Osborn*, 1980; *Moum*, 1990].

On the basis of laboratory observations, *Osborn* [1980] used 0.15 as an upper bound of the flux Richardson number yielding an upper bound of Γ equal to 0.2. *Moum* [1990] pointed out that Γ has a variation range of 0.1–0.4 by comparing the dissipation measurements and the temperature variance measurements. Because a $\Gamma = 0.2$ is still the choice of many authors [*Gregg*, 1987; *Smyth et al.*, 1996b], we use a constant $\Gamma = 0.2$ throughout this study.

3.3.3. Vertical velocity. Two methods are used to calculate the vertical velocity: one uses divergence

of horizontal velocity and the other uses isopycnal displacements.

In the first method,

$$w = w_0 - \int_{z_0}^{z} (\frac{\partial u}{\partial x} + \frac{\partial v}{\partial y})dz. \qquad (9)$$

The variable $z_0 = 0$, the sea surface, is the reference depth of the integration, and w_0 is the vertical velocity at z_0 and is assumed to be zero over the 3-day timescale. The horizontal gradients of the velocities are calculated with the linear fit. The divergence between 0–20 m is assumed to be constant. A tidal removal process [*Feng et al.*, 1998] is applied before the velocity gradient calculation. This process does not noticeably change the linear fit results but can reduce the variances in the residual and the error estimations.

The other method assumes adiabatic motion in the density equation, that is,

$$w \frac{\partial \rho}{\partial z} = -\frac{\partial \rho}{\partial t} - u \frac{\partial \rho}{\partial x} - v \frac{\partial \rho}{\partial y}. \qquad (10)$$

Variable ρ is the water density; the gradients of ρ are calculated from the linear fit. This method is used below the mixed layer depth, which is defined as equivalent to a 0.167 kg m^{-3} density change from the surface [*Sprintall and Tomzak*, 1992]. In the mixed layer, the vertical velocity is assumed to be linearly decreasing to zero at the sea surface.

There is qualitative agreement between the two (rather noisy) vertical velocity estimates. In practice, we average the two estimates weighted by their standard errors.

3.3.4. Diapycnal velocity. There are three methods to calculate the diapycnal velocity across an isopycnal depth from the available data.

1. Use the definition, that is,

$$w_e = \frac{dh}{dt} + w|_{-h}. \qquad (11)$$

Variable h is the isopycnal depth; $dh/dt = \partial h/\partial t + u|_{-h}\partial h/\partial x + v|_{-h}\partial h/\partial y$, which can be calculated by using the linear fit of the R/V *Wecoma* data, and $w|_{-h}$ is the vertical velocity from the divergence integration. From the Bootstrap analysis, the errors in the estimation of either term on the right-hand side of (11) are big enough to mask the signals. Also, the diapycnal velocity sometimes evolves with the diurnal processes, which are not resolved in the 3-day linear fit. Therefore this method is not used in this study.

2. Use the mixed layer turbulent kinetic energy equation [*Niiler and Kraus*, 1977]:

$$w_e \Delta b h(1 - sRi_b^{-1}) = 2mu_*^3 + \frac{h}{2}((1+n)B_0 -$$
$$(1-n)|B_0|) + ((h - \frac{2}{\gamma}) + (h + \frac{2}{\gamma})e^{-\gamma h})rR_S(0), \qquad (12)$$

where $\Delta b = -g(\overline{\rho} - \rho|_{-h})/\rho_0$, $\overline{\rho}$ is the mean potential

density above the isopycnal depth, $\rho|_{-h}$ is the potential density at the isopycnal depth, Ri_b is the bulk Richardson number, u_* is the friction velocity of the wind stress, B_0 is the surface buoyancy flux, $rR_S(0)$ is 38% of the

solar radiation (short-wave), γ^{-1} is 22.1 m according to the double exponential transmission profile observed during COARE IOP [*Siegel et al.*, 1995; *Cronin and McPhaden*, 1997], and m, n, and s are the efficiency
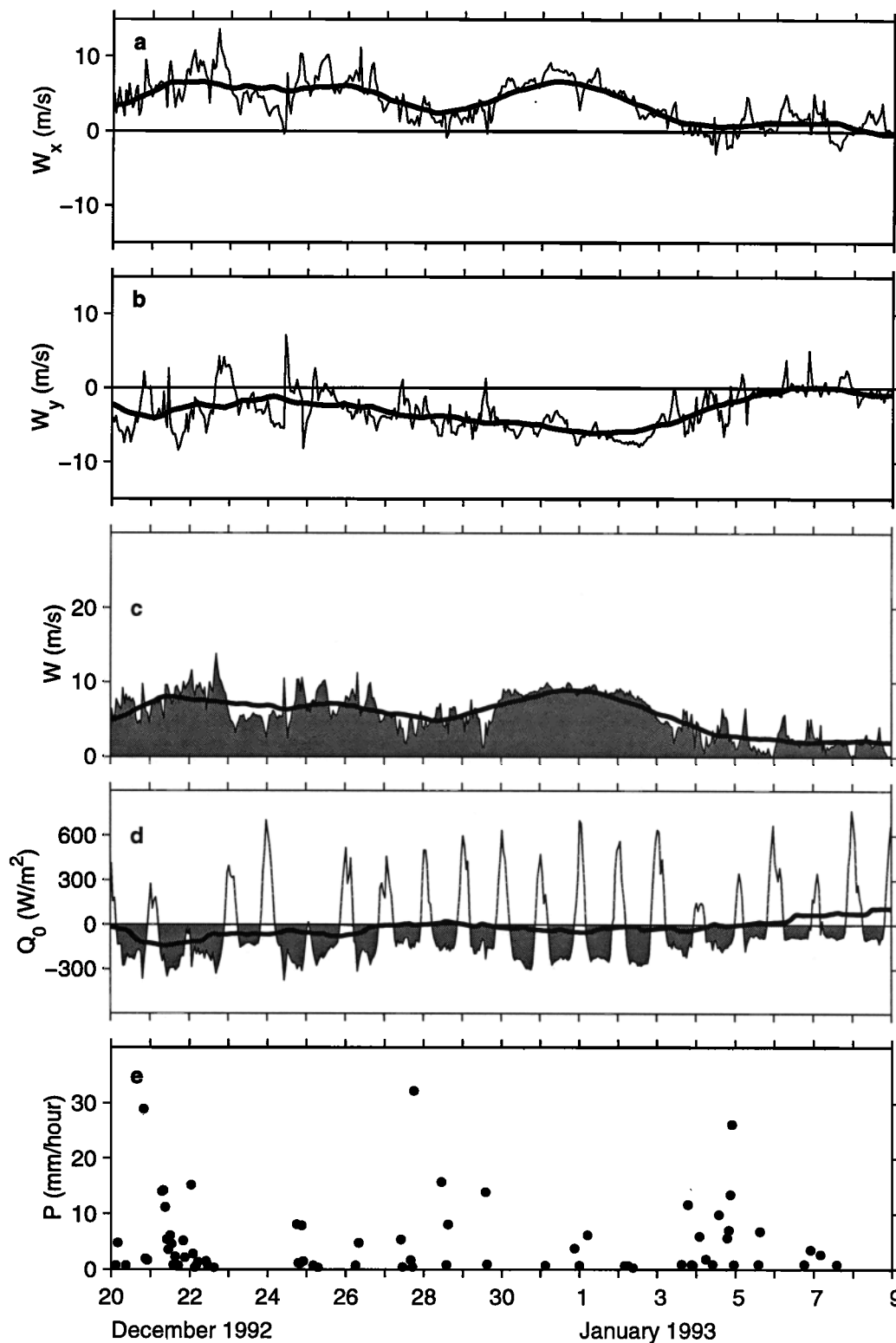
Figure 2. Time series of wind speed and air-sea fluxes: (a) eastward wind speed, (b) northward wind speed, (c) total wind speed, (d) net surface heat flux, and (e) rain rate. The bold lines in Figures 2a - 2d are 3-day moving averages.

factors. All the terms in the equation can be calculated; however, there are uncertainties in the efficiency factors, which we can estimate by comparison with the next method.

3. Use the density conservation equation [McDougall and You, 1990]:

$$w_e \frac{\partial \rho}{\partial z} = \frac{\partial}{\partial z}\left(K_\rho \frac{\partial \rho}{\partial z} + \frac{\alpha R_S(z)}{\rho_0 C_P}\right), \qquad (13)$$

where α is the thermal expansion coefficient. The first term on the right-hand side is due to the vertical gradient of the turbulent flux, and the second term is due to the vertical gradient of the penetrating solar radiation (Godfrey et al., personal communication, 1996). In Appendix B, we give a brief discussion about the equivalency between the density conservation method and the definition of the diapycnal velocity, (11); also, we give the rationale for including both the turbulent flux and diapycnal advection in the budget calculation.

In our study, we use the microstructure data for the calculation of diapycnal velocity. The second term on the right-hand side of (13) is two magnitudes smaller than the first term for the isopycnal depth we select. Neglecting the second term on the right-hand side and using the expression for K_ρ, (13) becomes

$$w_e = \frac{\Gamma}{N^2} \frac{\partial \epsilon}{\partial z},$$

which we evaluate from the microstructure data.

4. Results

4.1. Overview

The time period for our study covers the December WWB period and the beginning of the January low-wind period (JLW) [Weller and Anderson, 1996]. There are three WWB peaks during this time period (Figure 2), with peak wind speed on December 22, December 25, and between December 31 and January 2. The timescale of one WWB peak is a few days. The gap between the first and second WWB peaks is so small that from the near 3-day analysis, they are described as one peak. It is referred to as the first WWB peak. The last WWB peak is referred to as the second WWB peak. During the WWB period, the ocean is losing heat to the atmosphere until the beginning of the JLW period (after January 4). The significant heat loss periods are roughly coincident with the WWB peaks. The average heat loss across the air-sea interface during this study period is 32 W m^{-2}.

The rainfall is very large during this time period (average 18.8 mm d^{-1}). Heavy rainfall occurs in the first WWB peak because the deep convection is right on top of the IFA. During the second WWB peak, the deep convection moves farther east and the rain rate is small in the IFA. This also results in less heat loss in the second WWB peak due to larger solar radiation than in the first WWB peak. The large rain rate on January 3-5 may be due to the westward propagating near 2-day
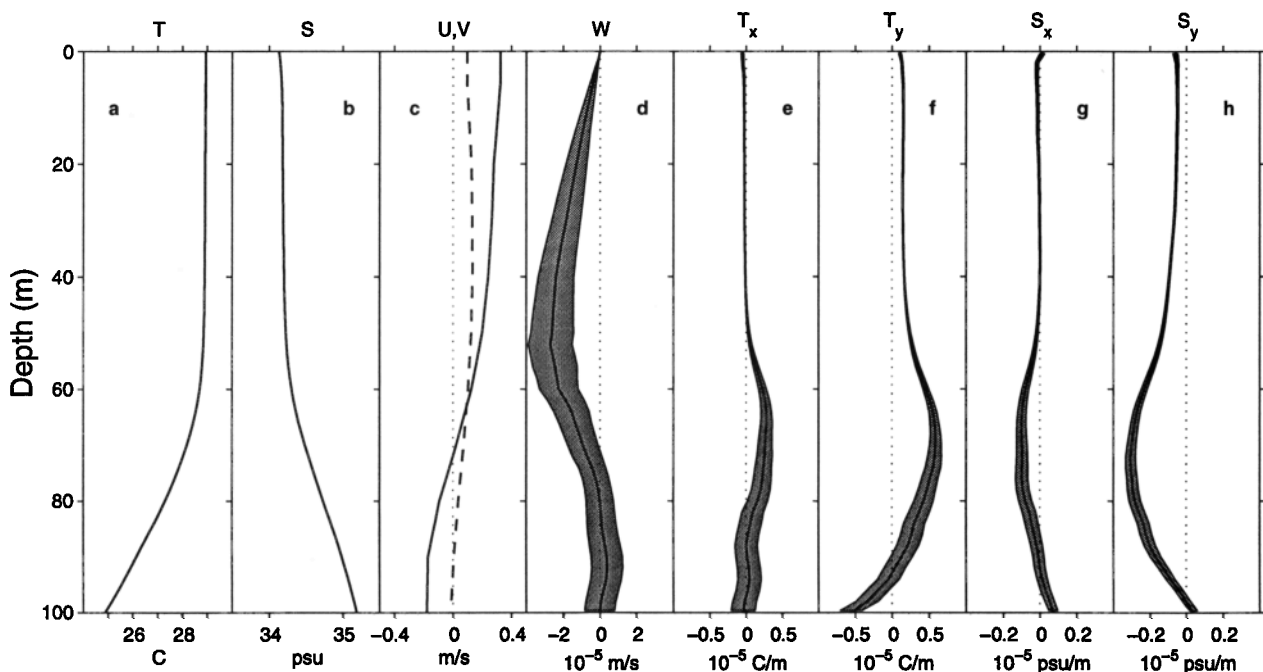
Figure 3. Cruise mean upper ocean properties at the R/V Wecoma crossover point: (a) temperature, (b) salinity, (c) eastward (solid) and northward velocities (dashed), (d) vertical velocity, (e) zonal and (f) meridional temperature gradients, and (g) zonal and (h) meridional salinity gradients. The shaded areas are the standard errors using bootstrap analysis. The errors in the mean temperature, salinity, and horizontal velocities are less than 0.05°C, 0.01 practical salinity unit and 1 cm s^{-1}, respectively.

oscillation near the end of the WWB period or due to localized convection [*Chen et al.*, 1996].

From the temporal mean profiles of the temperature and salinity (Figure 3), the surface layer is well mixed down to about 60 m. Both temperature and salinity gradients are important in stratifying the layers below 60 m. The mean zonal current (u) is toward the east ($\approx$ 30 cm s^{-1}) in response to the WWB in the surface layer. The subsurface current below 70 m is toward the west representing the remnant of the South Equatorial Current (SEC), which is sandwiched between the eastward flowing surface current and the Equatorial Undercurrent [*Eldin et al.*, 1994; *Huyer et al.*, 1997]. The meridional component (v) of the mean current is much smaller and has a northward tendency in the mixed layer ($\approx$ 10 cm s^{-1}). The mean vertical velocity is downward during this time period, with a peak velocity of more than -2×10^{-5} ms^{-1} at 50 m. Temperature and salinity are dominated by the meridional gradients in the mixed layer with increasing temperature and decreasing salinity toward the north (Figure 3). The mean meridional gradients of temperature and salinity below the mixed layer depth have signs consistent with a geostrophically balanced mean current. The zonal gradients in both the temperature and salinity are smaller than the meridional gradients.

Figure 4 shows the temporal evolution of the u and v components of the velocity and the temperature and salinity at the crossover point above 100 m from the linear fit. The low-pass filtered data (removing the diurnal and semidiurnal tides) from the 5 m WHOI current meter is used to interpolate the velocity from 20 m to the sea surface. The u component is eastward in the mixed layer during all the time in response to the WWB. Both the surface eastward flow and subsurface westward flow accelerate during the two WWB peaks. The acceler-
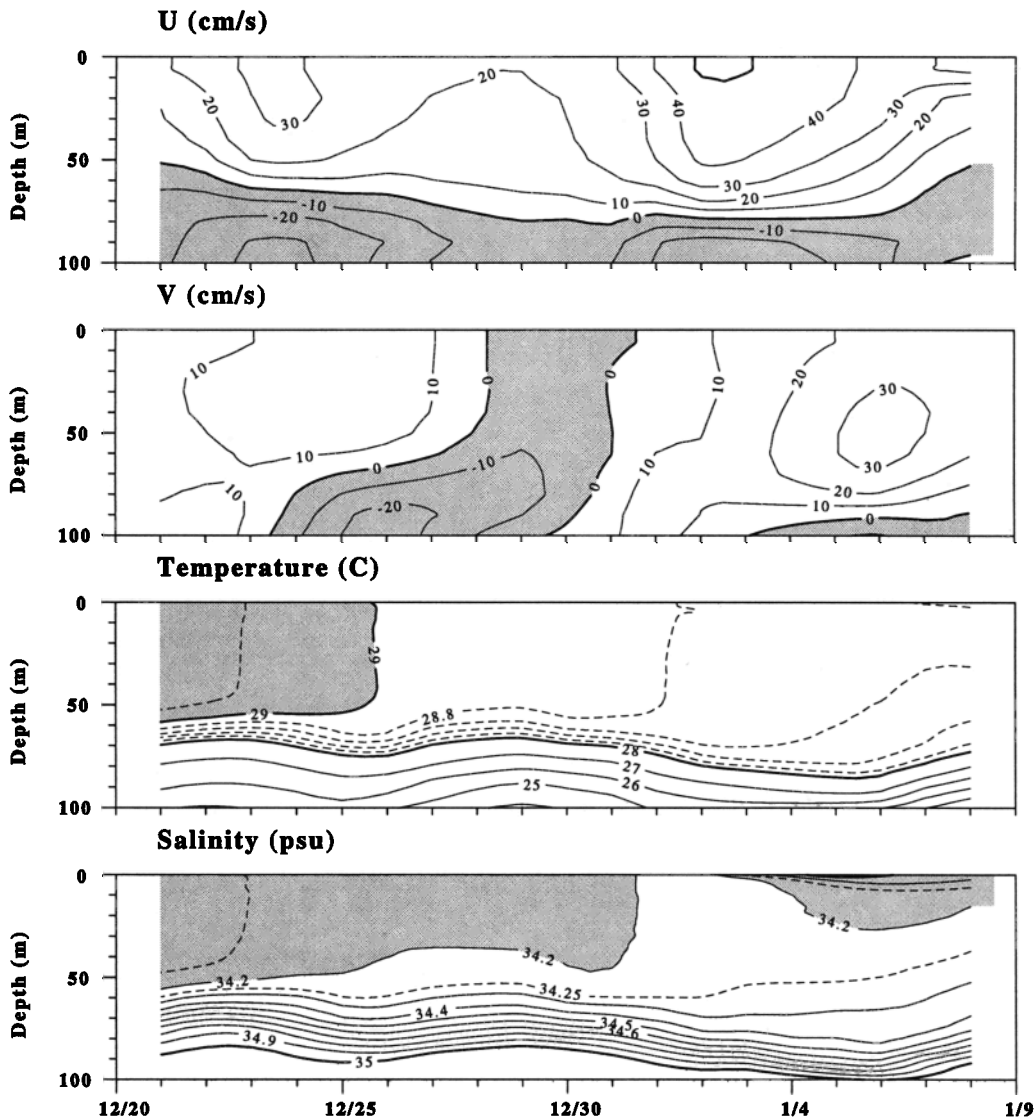
Figure 4. Temporal evolution of eastward and northward velocities, temperature, and salinity at the R/V *Wecoma* crossover point. The negative velocities (westward and southward), temperature above 29°C and salinity below 34.2 psu are shaded.

ation of the subsurface flow may be due to pressure gradient and inertial motions [Smyth et al., 1996a]. The surface layer v component is northward most of the time and has a northward acceleration a few days after the eastward acceleration of the u component, which is due to inertial motions [Smyth et al., 1996a]. There are indications of vertical propagation from the structure of the v component, also seen in the moored observations (S. Anderson, personal communication, 1997). Thus it seems possible that inertial motions are of importance in the upper ocean heat and salt budgets because of their effects on shear and mixing.

The mixed layer temperature decreases in response to the WWB (Figure 4). During the JLW, the top few meters are warmed up, and the isotherms below 50 m shoal so that there is a trend of increasing stratification in the surface layer. Smyth et al. [1996b] argued that the turbulence generated by the strong shear between the surface wind-driven current and subsurface SEC might also contribute to this stratification process. The 28°C depth is almost coincident with the $\sigma_\theta = 22$ kg m^{-3} depth (also the 34.5 psu depth) in the R/V Wecoma data, which is also the case from the R/V Moana Wave data [Smyth et al., 1996b]. Generally, the 28°C depth deepens gradually from 70 m to more than 80 m in response to the WWB, and it shoals to 70 m after the WWB. Note that the lower boundary of the surface layer eastward flow in the u component also has

similar vertical displacements. Despite the heavy rainfall during the first WWB peak, the surface salinity slightly increases except during the JLW when shallow fresh water pools develop in the top few meters.

During most of the time, there is a northward temperature gradient in the mixed layer (Figure 5). Significant gradients are found during December 25-26, 1992, and after January 3, 1993. The southward salinity gradient has maxima during similar time periods in the mixed layer (Figure 6). In the mixed layer, the zonal temperature and salinity gradients are generally smaller than the meridional. Below the mixed layer depth, the internal wave signals introduce significant errors in the fixed depth gradient calculations (Figure 3). Thus it is more difficult to calculate heat and salt advection below the mixed layer in the fixed thickness analysis; an isopycnal depth may be more useful as a lower boundary.

4.2. Heat and Salt Balances Above a Fixed Depth

Results from the cruise mean analyses are shown in Figure 7 for heat and Figure 8 for salt. In Figure 7, the whole water column above 100 m is losing heat at a rate near 2 W m^{-3}. Above 60 m, the meridional advection is a big contributor to the heat loss, and the zonal and vertical advection terms are much smaller. According to (1), the vertical gradient of the penetrating solar radiation flux is subtracted from the sum of
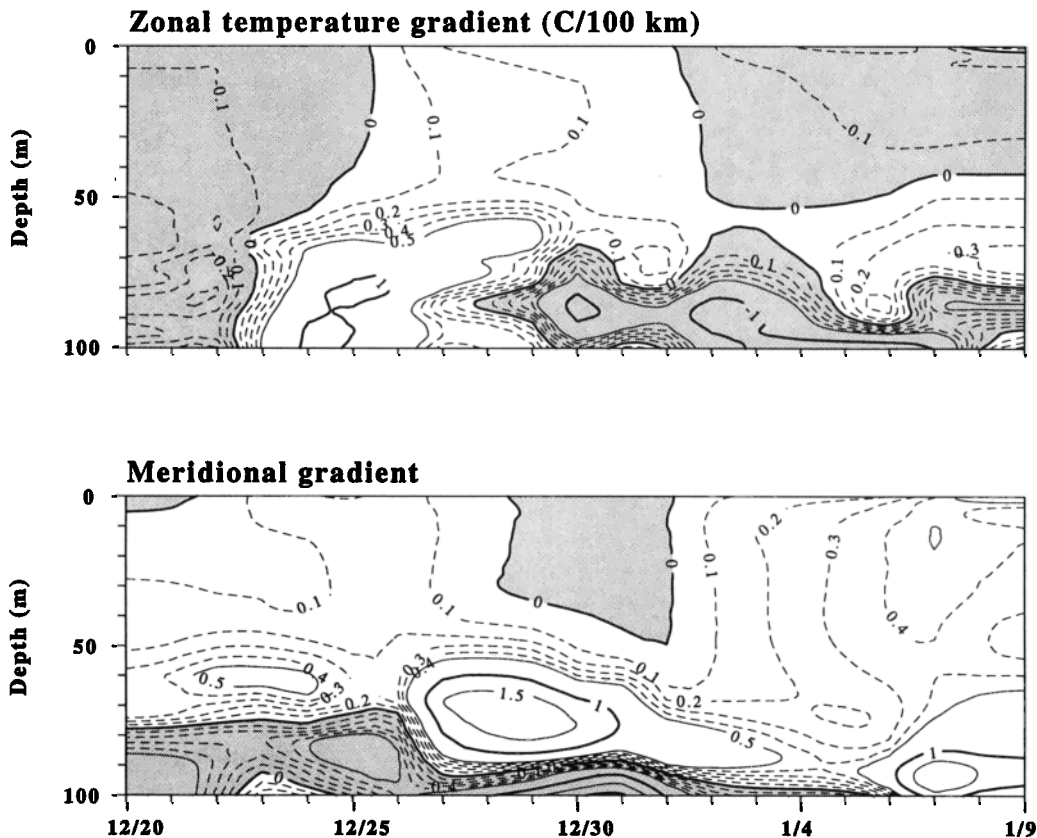
Figure 5. Temporal evolution of zonal and meridional temperature gradients from the linear fit. Positive gradients are toward the north and east. Negative gradients are shaded.

Zonal salinity gradient (psu/100 km)

Meridional gradient
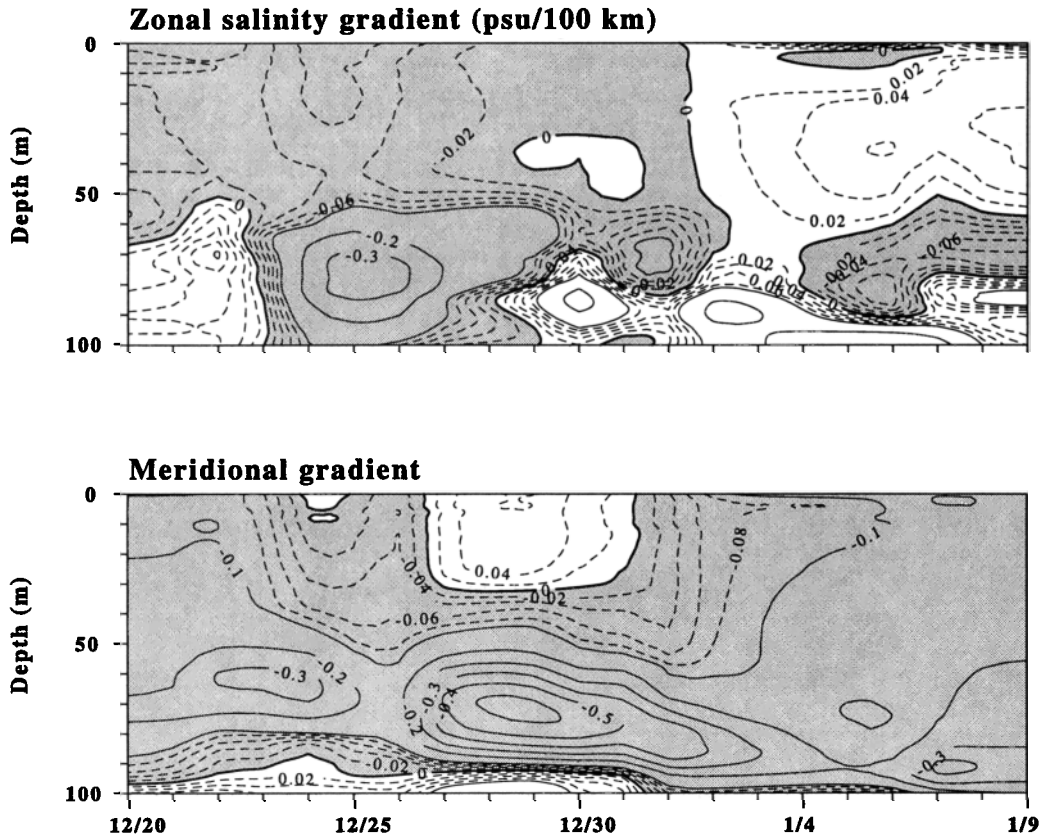
Figure 6. Temporal evolution of zonal and meridional salinity gradients from the linear fit. Positive gradients are toward the north and east. Negative gradients are shaded.
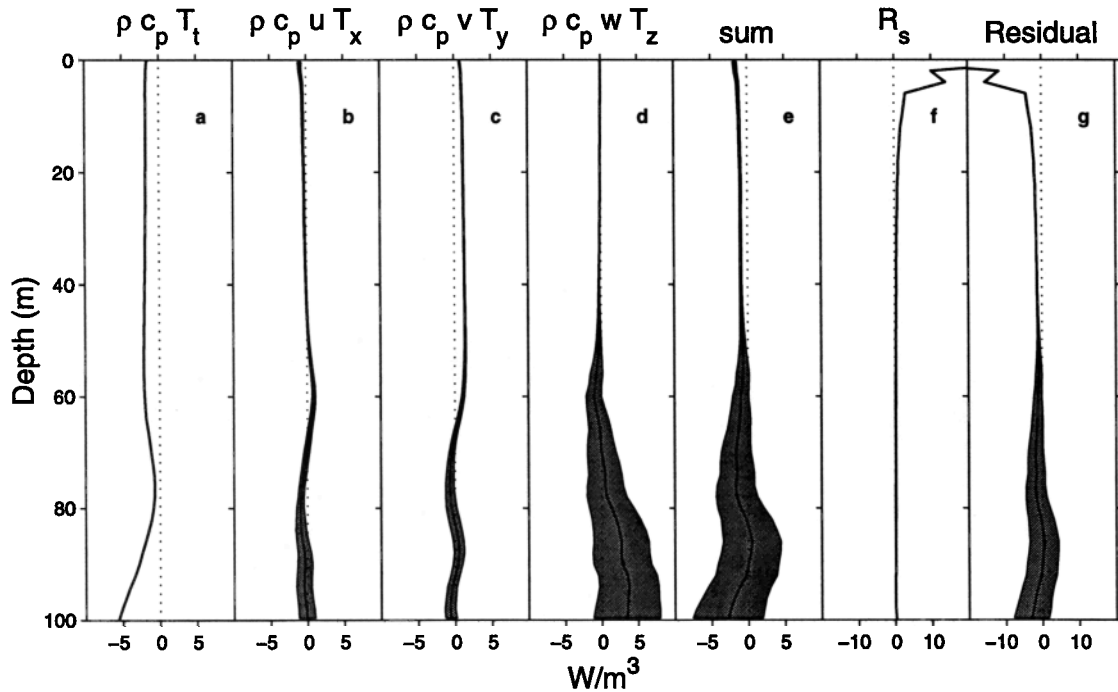
Figure 7. Cruise mean of heat tendency equation (1): (a) temporal rate of heat content, (b) zonal, (c) meridional and (d) vertical advections of heat, (e) the summation of the above four terms, (f) the penetrating solar radiation, and (g) the residual between Figures 7e and 7f, which is $-dF_T(z)/dz$.
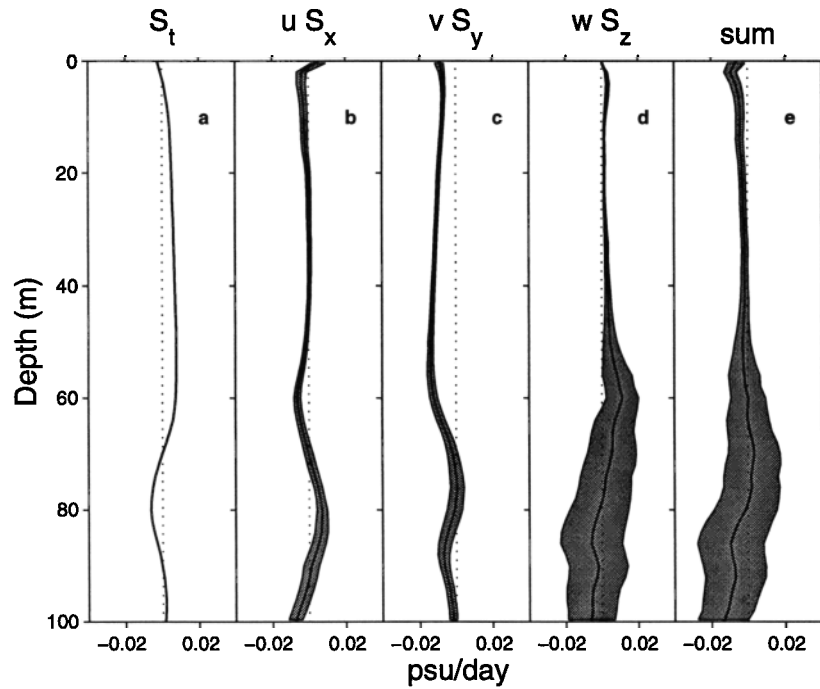
Figure 8. Cruise mean of salt tendency equation (2): (a) temporal rate of salinity change, (b) zonal, (c) meridional and (d) vertical advection of salt, and (e) the summation of the above four terms, which is also $-dF_S(z)/dz$.
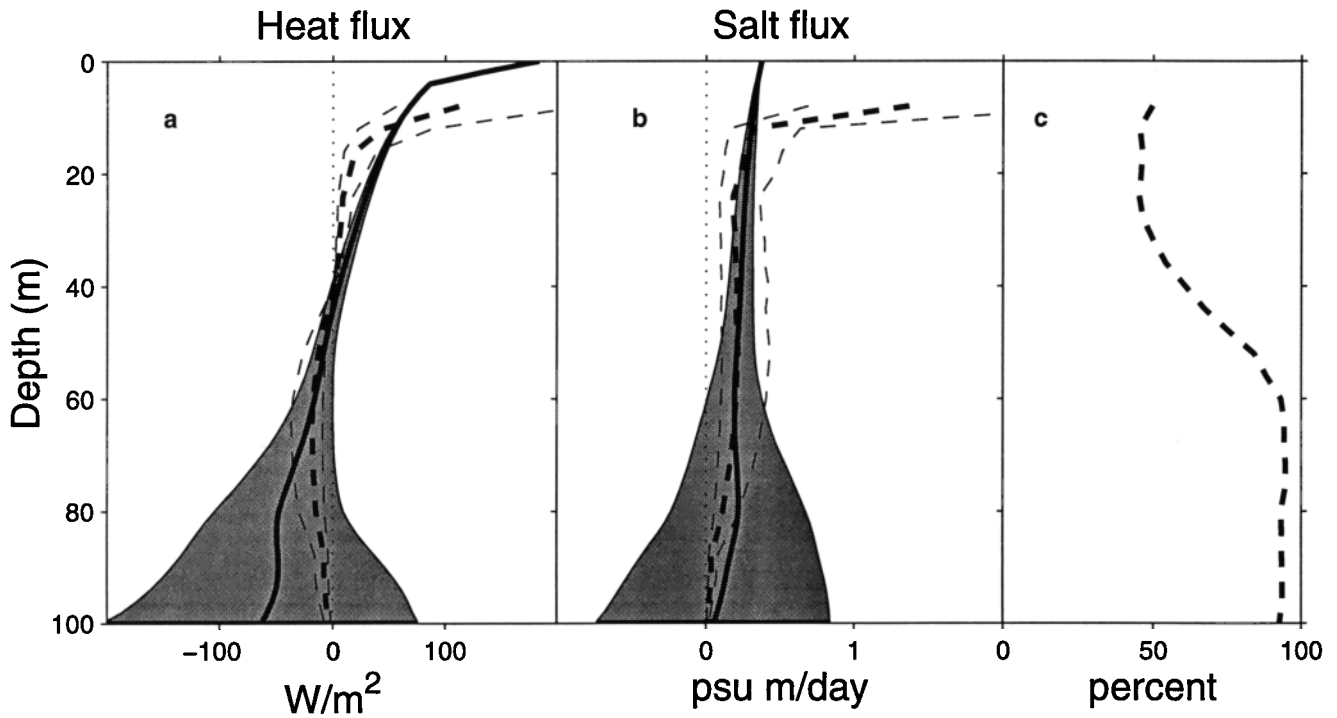
Figure 9. Cruise mean turbulent fluxes: (a) $F_T(z)$ derived from the residual of the advection terms (bold solid line) and that derived from the microstructure measurement assuming $\Gamma = 0.2$ (bold dashed line) and $\Gamma = 0.1$ and 0.4 (light dashed lines). The shaded area is the standard error of the advection terms integrated from sea surface. (b) The same as Figure 9a but for $F_S(z)$. (c) The percentage of hourly microstructure data available for the calculation with $N^2 \geq N_{min}^2 = 3 \times 10^{-6}$ s^{-2}.

the temporal and advection terms. The residual, or the remaining term, then includes the vertical gradient of the vertical turbulent flux, $-dF_T(z)/dz$, and the errors (Figure 7). The R/V *Vickers* observations have missed some of the energy spectrum near the sea surface (S. Anderson, personal communication, 1997), so there is a secondary maximum near about 6 m (Figure 7). This effect is not adjusted, because it does not affect the results below 6 m.

Knowing the surface turbulent heat flux $F_T(0)$ (184 W m^{-2}) from the WHOI and R/V *Moana Wave* data, the residual of Figure 7 is integrated from the surface downward (equation (3)). In this way, the vertical profile of the turbulent heat flux, $F_T(z)$, is calculated (Figure 9a). The $F_T(z)$ derived from the residual of the advection calculation and the $F_T(z)$ calculated from (8) using the microstructure data agree within 10 W m^{-2} between 40 and 70 m when selecting $\Gamma = 0.2$ (Figure 9a). Thus a fixed-thickness analysis of the heat budget is not sensitive to the lower depth selection within this depth range in the cruise mean sense. There is significant bias between the two flux estimates below 70 m.

The salinity in the mixed layer slightly increases during cruise 2 (Figure 8). As in the heat balance case, the zonal and vertical advection terms are small in affecting the surface layer. The meridional advection brings more salt to the IFA mixed layer than the salinity change. This difference, the residual in Figure 8, has to be balanced by the vertical gradient of the turbulent fluxes according to (2). Assuming that the turbulent flux F_S is equal to the result from microstructure data at 50 m, the residual is integrated to obtain $F_S(z)$. In this way, the predicted turbulent flux at the sea surface is 0.38 psu m d^{-1} (Figure 9b), which is equivalent to 11.1 mm d^{-1} precipitation minus evaporation rate. Using the WHOI evaporation data, the predicted average precipitation is 15.4 mm d^{-1} during our study time period. This precipitation number is consistent with the R/V *Wecoma* optical rain gauge measurements; the R/V *Moana Wave* rain rate is about 20% higher than this prediction, which may be partly due to spatial variations [*Bradley and Weller*, 1997]. The $F_S(z)$ compares well with that derived from the microstructure data in the depth range of 40–70 m (Figure 9b). The bias below 70 m is less than in the heat flux.

The results from the microstructure data seem to underestimate the turbulent fluxes between 20 and 40 m (Figure 9). When $N^2 < N^2_{\min} = 3 \times 10^{-6}$ s^{-2}, N^2 is assumed to be equal to $N^2_{\min}$ in calculating the turbulent fluxes from the microstructure data [*Smyth et al.*, 1996b]. Note that only about half of the hourly microstructure data have $N^2 \geq N^2_{\min}$ above 50 m (Figure 9c), so that the estimate from the microstructure data may be biased (W. Smyth, personal communication, 1996). The 10 m microstructure data are contaminated by the ship wake.

In the following temporal evolution analysis of the heat and salt balances, we pick h=50 m as the lower

boundary. This selection provides a compromise between minimizing errors in the advection calculations and maximizing the information of the mixed layer.

During the 19–day time period (from day 355 to the center time of the last 3-day fit), the heat content in the upper 50 m decreases by 150 MJ m^{-2} (equivalent to a flux of 92 W m^{-2} for 19 days). Over this time period, only about one third of this heat loss is due to the air-sea flux, 52 MJ m^{-2} (32 W m^{-2}) (Figure 10). We see that the total advection term also contributes to the cooling of the surface layer and has a cumulative effect of 70 MJ m^{-2} (43 W m^{-2}), which is larger than the air-sea flux during this time period. The penetrating solar radiation term has a cumulative effect of 13 MJ m^{-2} (8 W m^{-2}). In Figure 10a, the turbulent flux term at 50 m is included in the residual. Without vertical turbulent flux, the residual is nearly 20 MJ m^{-2}.

Comparing the residual with the turbulent flux at 50 m, the largest discrepancy occurs during the first WWB peak, with the ocean losing more heat than which that can be mixed downward. This could be due to the underestimates of the turbulent flux, the sea surface heat loss, or the advective cooling. Near the end of this time period, the situation reverses (Figure 10b, also see Figure 13). As a cruise mean, the residual compares well with the turbulent flux at 50 m, and the heat budget is balanced to 2 W m^{-2} (Figure 10b). The standard error in the heat advection terms for the whole time period is 11 W m^{-2}, which is comparable with errors in other terms (Table 1). However, the errors in the advection terms may have been overestimated (Appendix A).

The combined precipitation and evaporation has a cumulative effect of 9.3 psu m (272 mm of fresh water; Figure 11a), tending to decrease the salt content in the upper 50 m; however, the salt content in this layer actually increases slightly by 4.7 psu m (-137 mm of fresh water). Most of the increase occurs during the first WWB peak. The advection terms play a major role in balancing this difference and account for a change of 7.6 psu m (-222 mm). However, the residual, 6.4 psu m (-187 mm), is still very large.

The turbulent flux has a cumulative effect of 4.2 psu m (-123 mm) and does not account for all the above residual. The imbalance is about 20% of the rain rate estimation from the R/V *Moana Wave*, as shown before. The error in the advection estimation can barely account for this imbalance (Figure 11b). Thus this imbalance can be due to an overestimation of the rain rate by 20% in the R/V *Moana Wave* data or due to the spatial variations of the rain rate [*Bradley and Weller*, 1997] or due to error in the vertical turbulent flux estimate.

As a cumulative result, the meridional advection dominates the total advection, 103 MJ m^{-2} (63 W m^{-2}) in the heat balance and 9.5 psu m (-278 mm) in the salt balance (Figure 12). The effects of the meridional advection terms are to decrease the temperature and increase the salinity in the surface layer after each of the two WWB peaks. This is due to the northward
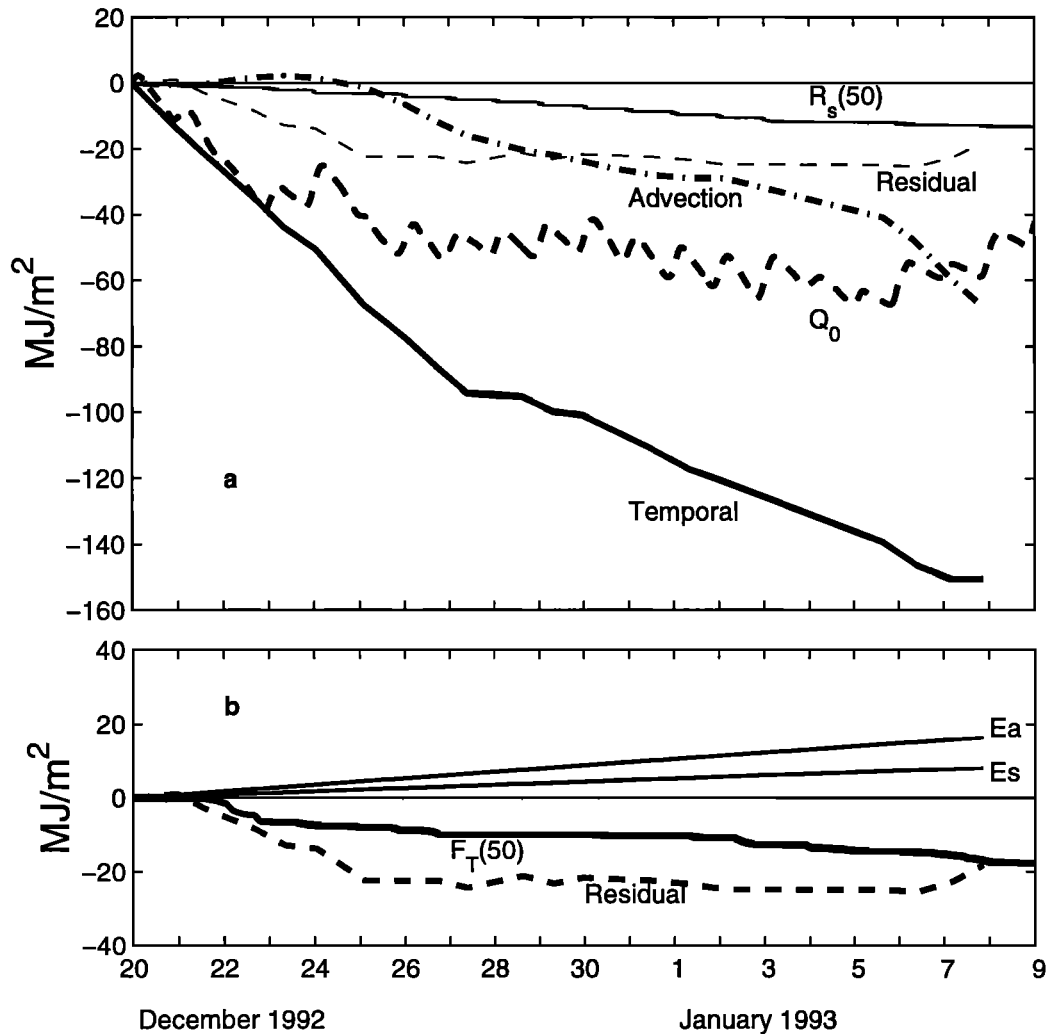
Figure 10. (a) Cumulative heat budget in the 0–50 m layer. The advection term includes the zonal, meridional, and vertical advection. The residual includes the vertical turbulent flux at 50 m and estimation errors. (b) The comparison between the residual in Figure 10a with the vertical turbulent flux estimate from the microstructure data. E_s (5 W m^{-2}) and E_a (11 W m^{-2}) are the cumulative errors in the surface heat flux and advection terms, respectively.

inertial current during these two time periods and is consistent with the observed northward propagation of frontlike features in both surface temperature and salinity [*Huyer et al.*, 1997]. During the JLW, when the net

Table 1. Comparison of Error Estimations of Different Terms.

Terms	Standard Error
Net surface heat flux [*Weller and Anderson*, 1996]	< 10
Turbulent heat flux at 50 m [*Smyth et al.*, 1996b]	10
Heat advection (present study)	11

Error estimations given in W m^{-2}.

surface heat flux tends to heat the surface layer, advection still causes the mean temperature in the water column to decrease (Figures 10 and 12).

Generally, zonal advection shows some eddylike behavior, but the net effects are small compared with meridional advection. The zonal salt advection is as important as the meridional advection until January 2 when the zonal salinity gradient changes sign and the current turns northeastward in the surface layer. Vertical advection is unimportant until the end of the cruise when the surface layer is stratified (Figure 12). The net effects of vertical advection are to increase the surface temperature and decrease the surface salinity; this is caused by the downward vertical velocity in this layer.

The instantaneous heat balance in the 0–50 m layer, using the near 3-day analysis, is shown in Figure 13. The temperature decreases all the time. The vertical flux, which includes the net surface heat flux, the pen-

Figure 11. (a) Cumulative salt budget in the 0–50 m layer. The advection term includes the zonal, meridional, and vertical advection. The residual includes the vertical turbulent flux at 50 m and estimation errors. (b) The comparison between the residual in Figure 11a with the vertical turbulent flux estimate from the microstructure data. E_a is the cumulative error in the advection terms.

etrating solar radiation at 50 m and the vertical turbulent flux at 50 m, is negative during most of the time except near the end of this time period. The advection cools the surface layer during the two northward advection time periods. The residuals are larger than in the cumulative results during some 3-day periods, with imbalances as large as 90 W m^{-2}. The large error, on the one hand, is caused by averaging over short time periods, so that the errors in the different terms are more than doubled the numbers listed in Table 1. However, the temporal variation term has standard error of about 20 W m^{-2}, which has been avoided by using the mean value instead of integrating the temporal gradient in the cumulative calculations (Appendix A). The instantaneous salt balance is not shown because the rain rate

is estimated only at one point, and the rain events are sparse in space [*Short et al.*, 1997].

4.3. Diapycnal Velocity

The entrainment process of the mixed layer can be seen from a comparison of the mixed layer depth and the $\sigma_\theta = 22$ isopycnal depth (Figure 14a). Both depths are calculated from the R/V *Wecoma* survey data so that they contain both temporal and spatial variations. The mixed layer depth is calculated using a density gradient criterion of 0.01 kg m^{-4} [*Lukas and Lindstrom*, 1991]. Note that there are two occasions that both the mixed layer depth and the isopycnal depth deepen with the occurrences of the WWB peaks, one during December 22-25 and the other between December 30 and January
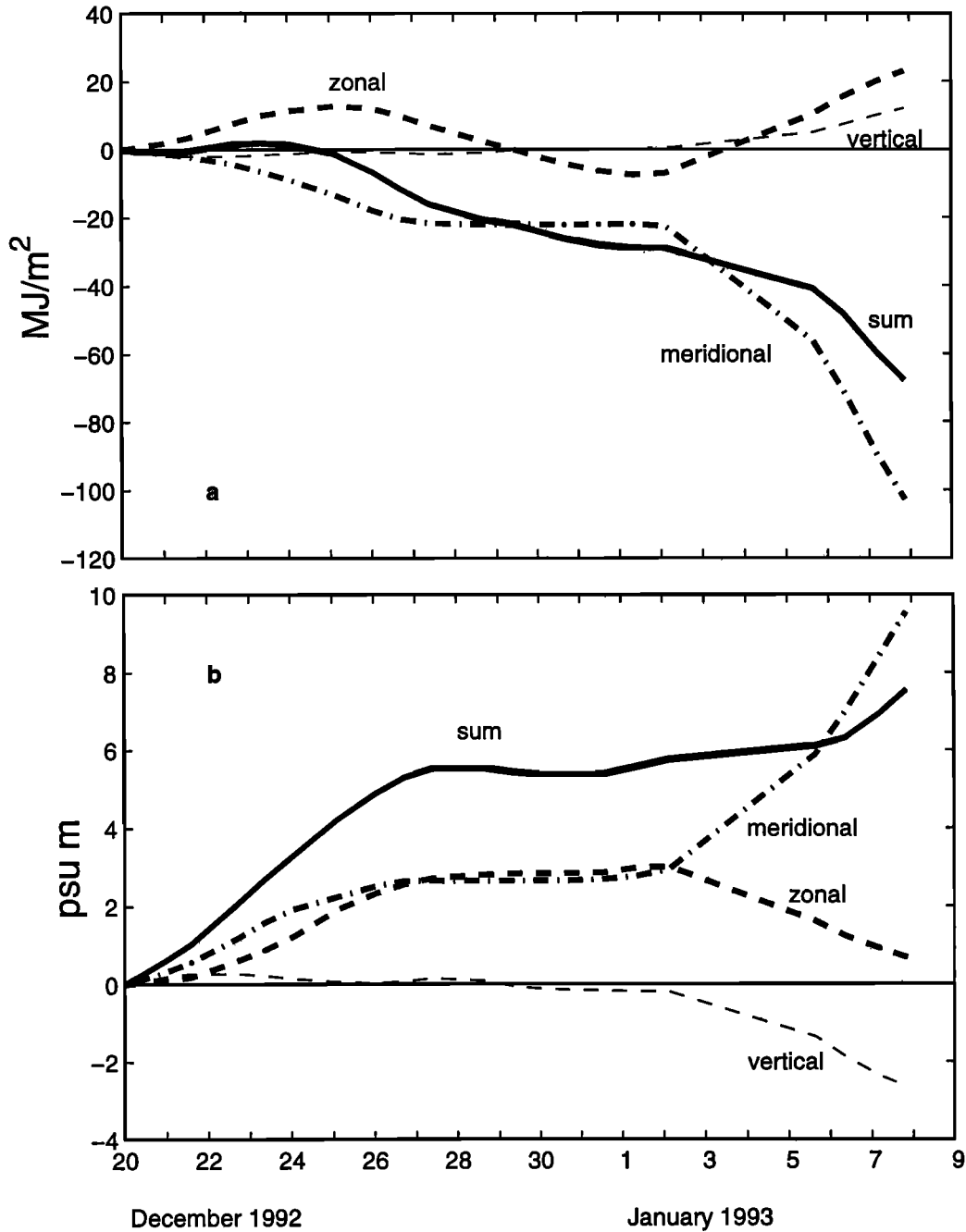
Figure 12. Cumulative effects of the zonal, meridional, and vertical advection in (a) heat and (b) salt balances in the upper 50 m layer.

2. Convergence in the surface layer (above $\sigma_\theta = 22$) may cause the deepening of the isopycnal depth during January 4-6 when the mixed layer shallows.

The isopycnal depth deepens to the north (tilts upward to the south) in response to the northward inertial current during December 27 to January 1 and after January 6 (Figure 14b). These southward tilts of the isopycnal depth may cause the meridional temperature and salinity gradients in the surface layer. The zonal gradient of the isopycnal depth is small most of the time, but it deepens toward the east in response to the first

WWB peak. This deepening may generate a pressure gradient in the zonal direction and thus be related to the acceleration of the subsurface SEC.

In the isopycnal boundary method, the σ_θ=22 isopycnal is used as the lower boundary of the surface layer. Because the layer above the σ_θ=22 isopycnal depth is not completely well mixed during the entire time period, both positive and negative diapycnal velocities may affect the properties of the surface layer.

Generally, the vertical gradients of the temperature, salinity, and potential density above the isopycnal depth
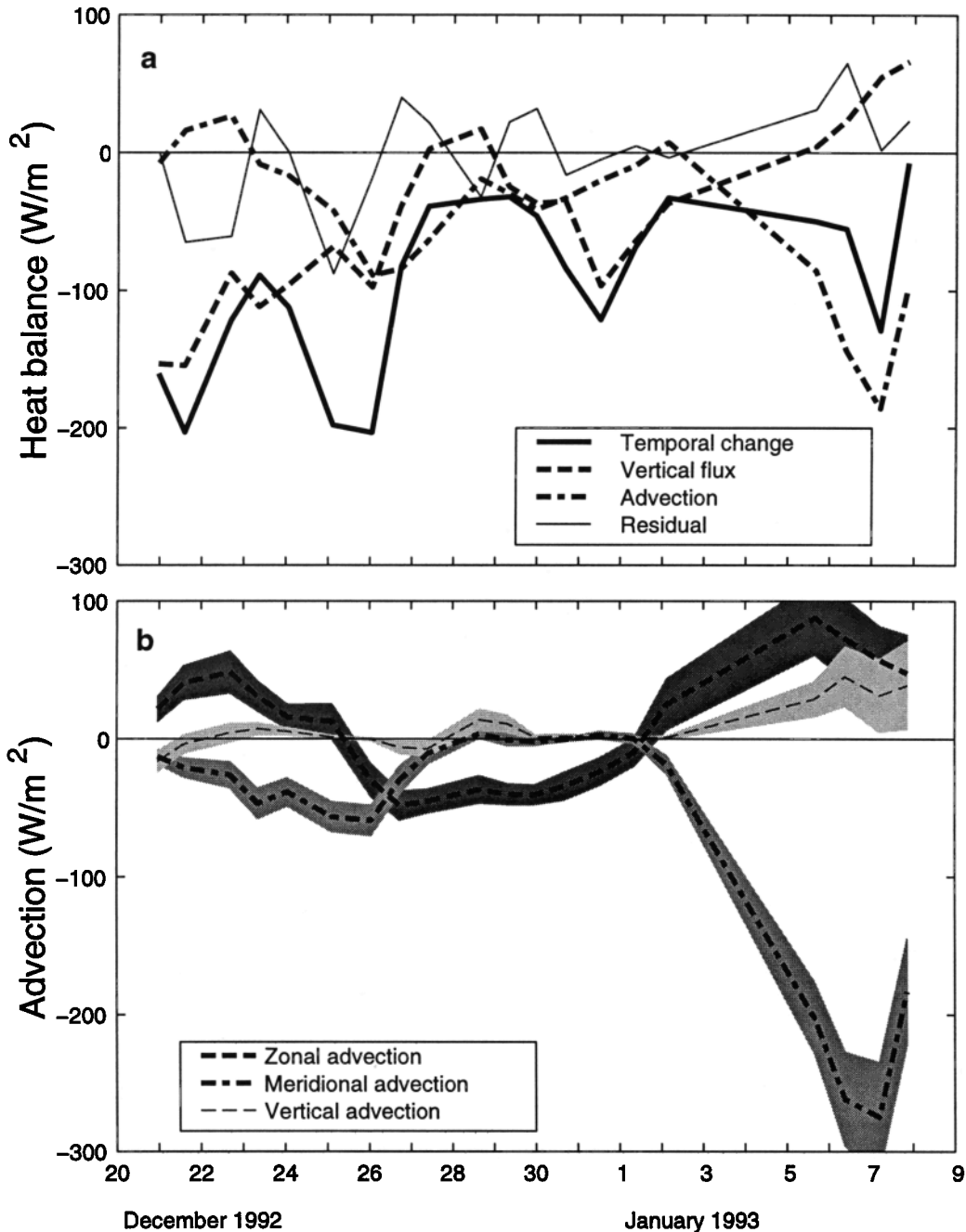
Figure 13. (a) Heat balance in the near 3-day analysis, and (b) the zonal, meridional, and vertical advection effects in the near 3-day intervals in the upper 50 m layer. The shaded areas represent the standard errors in the estimates.

are smaller than those below the isopycnal. Because diapycnal advection is an upwind process, positive w_e, equivalent to the entrainment in the mixed layer analysis, is more efficient in modifying the surface layer than negative w_e (detrainment). Thus we define the ratio between the vertical gradients above and below the isopycnal as the efficiency ratios between negative and positive w_e (detrainment and entrainment) (Figure 15). Using a linear fit, the detrainment of the temperature is 84% as efficient as the entrainment. The salinity efficiency is 75%, and the density efficiency is 79%.

Significant positive w_e occurs during the WWB peaks, from both the density conservation method and the entrainment calculation using the Niiler-Kraus formula (Figure 16). The result from the Niiler-Kraus formula is dominated by the diurnal cycle. After the last WWB peak, there is substantial negative w_e using the density conservation method; this may be due to the remnant of turbulence near the $\sigma_\theta = 22$ depth [Smyth et al., 1996b]. Using $n = 0.16, m = 0.24$, and $s = 0.24$, the estimated cumulative entrainment using the Niiler-Kraus formula and the cumulative positive w_e using the
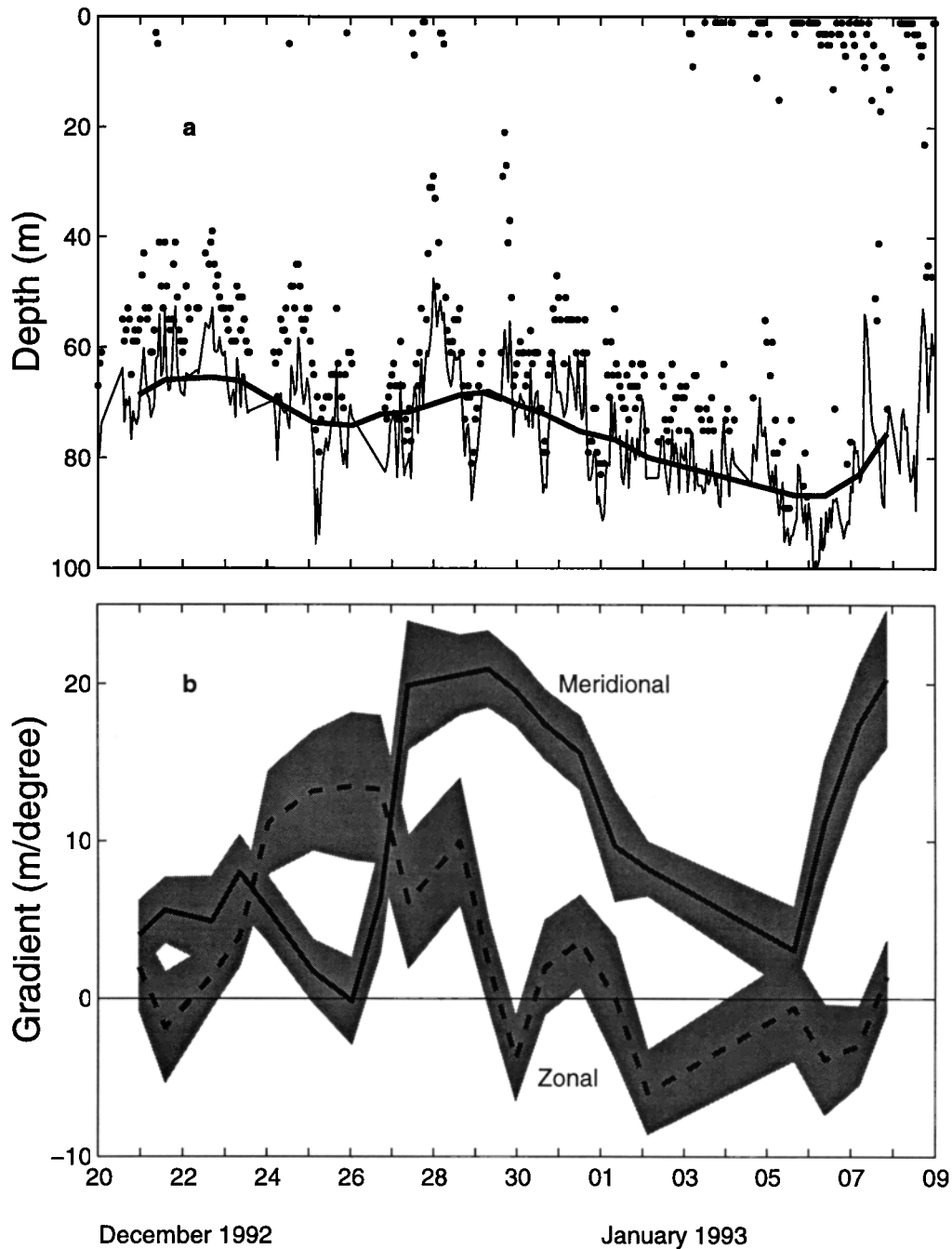
Figure 14. (a) The hourly mixed layer depth (circles) and the $\sigma_\theta = 22$ isopycnal depth (solid line) from the R/V *Wecoma* data. The bold line represents the linear fit mean of the isopycnal depth. (b) The eastward (dashed) and northward (solid) gradients of the isopycnal depth. Units (m/degree) are per degree longitude and latitude respectively. The shaded areas represent the standard errors in the estimation.

density conservation method are very close. When the isopycnal is close to the mixed layer depth, the entrainment velocity using the Niiler-Kraus formula can depict the positive diapycnal velocity by selecting the efficiency factors. The diapycnal velocity determined from the microstructure data depicts the turbulent structure near the isopycnal depth; it equally represents the positive and negative diapycnal velocities. Therefore, in our calculations of the heat and salt balances above an

isopycnal depth, the diapycnal velocity calculated from the microstructure data is used.

4.4. Heat and Salt Balances Above $\sigma_\theta = 22$

The mean temperature above the $\sigma_\theta = 22$ isopycnal decreases by 0.7°C during our study time period (Figure 17a). This temperature decrease is about equally accounted for by the net sea surface heat flux, the horizontal advection, and the vertical processes at the iso-
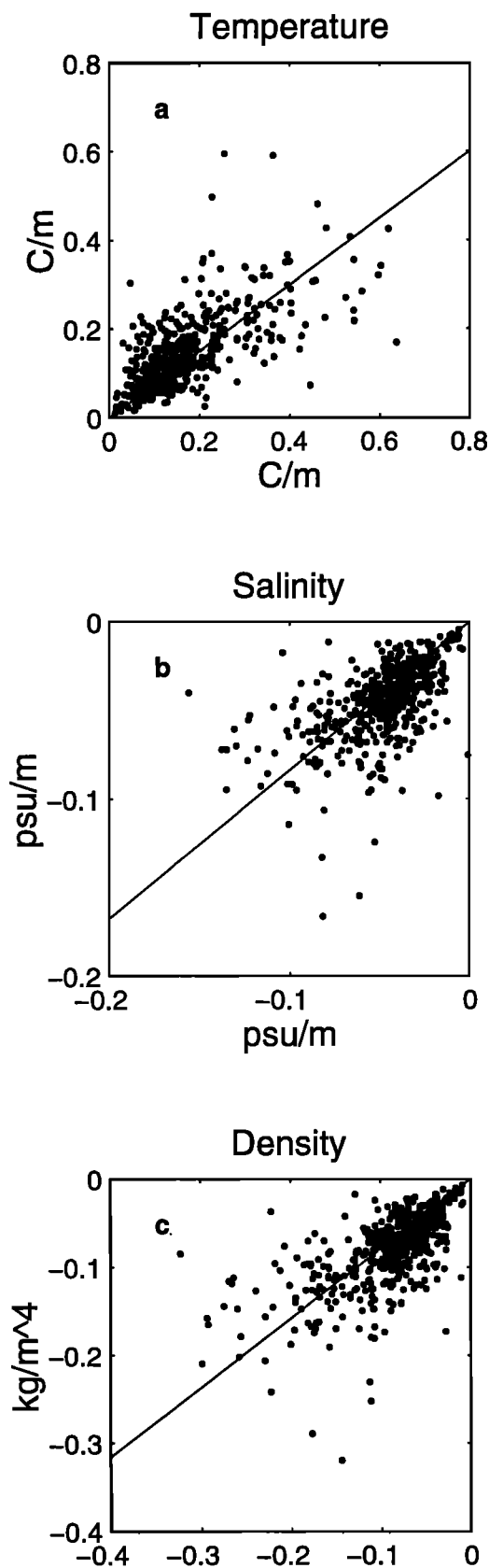
Figure 15. Comparison of the vertical gradients of the (a) temperature, (b) salinity, and (c) density above (Y axes) and below (X axes) the $\sigma_\theta = 22$ isopycnal depth from the R/V *Wecoma* data. The solid lines are the linear fits of the ratios.

pycnal surface which are represented by the residual in Figure 17a. The penetrating solar radiation is very small.

From Figure 17b, the diapycnal turbulent flux occurs only at the end of the time period when the mixed layer is shallow and there is still extensive turbulence near the isopycnal depth [*Smyth et al.*, 1996b]. Diapycnal advection occurs during the two WWB peaks with a cumulative effect almost as important as the diapycnal turbulent flux. Considering a mean isopycnal depth of 76 m, the diapycnal flux has an effect of 17 $W\,m^{-2}$ and the diapycnal advection has an effect of 13 $W\,m^{-2}$, while the penetrating solar radiation only has an effect of 2.4 $W\,m^{-2}$, during the 19-day time period. Adding these up, there is a total of 32 $W\,m^{-2}$ of heat entering across the $\sigma_\theta = 22$ isopycnal. The imbalance is near 0.06°C (about 10 $W\,m^{-2}$).

The temporal variation of mean salinity above $\sigma_\theta = 22$ is only of the order of 0.1 psu, which is smaller than the temperature in terms of its effect on the density (Figure 18a). The surface freshwater input tends to decrease mean salinity by 0.12 psu during this time period; the advection terms tend to increase the mean salinity by 0.13 psu. Thus the increase of mean salinity (0.087 psu) is almost coincident with the residual in Figure 18a. The diapycnal turbulent flux and diapycnal advection are almost equally important (Figure 18b), as in the temperature case. The sum of these two terms does not account for the above residual, and the imbalance is near 0.03 psu. Multiplied by the mean water depth of 76 m, this is comparable to the imbalance from the fixed thickness method. Thus the isopycnal boundary method yields the same rain rate estimate, 15.4 $mm\,d^{-1}$, as in the fixed thickness method. The standard errors in the rain rate estimations from the ocean budget are equivalent to 4 $mm\,d^{-1}$ in both methods.

5. Discussion

It has long been assumed that the horizontal advection effect on the heat balance in the center of the warm pool region is negligible. However, during the December 1992 WWB event, the advection effect (43 $W\,m^{-2}$) is more important than the air-sea flux in cooling the surface layer at the center of the IFA from the IOP observations. A similar short-term strong advection event is identified near the equator [*Cronin and McPhaden*, 1997]. Thus, for some short time periods, advection is important in the surface layer heat balance. In the total advection, the meridional advection term is dominant in both heat and salt balances during this 19-day period (Figure 12). There are two meridional advection events during this time period related to the two occurrences of WWB peaks. Thus the WWB-related eastward jet and inertial motions have significant impact on the heat and salt balances.
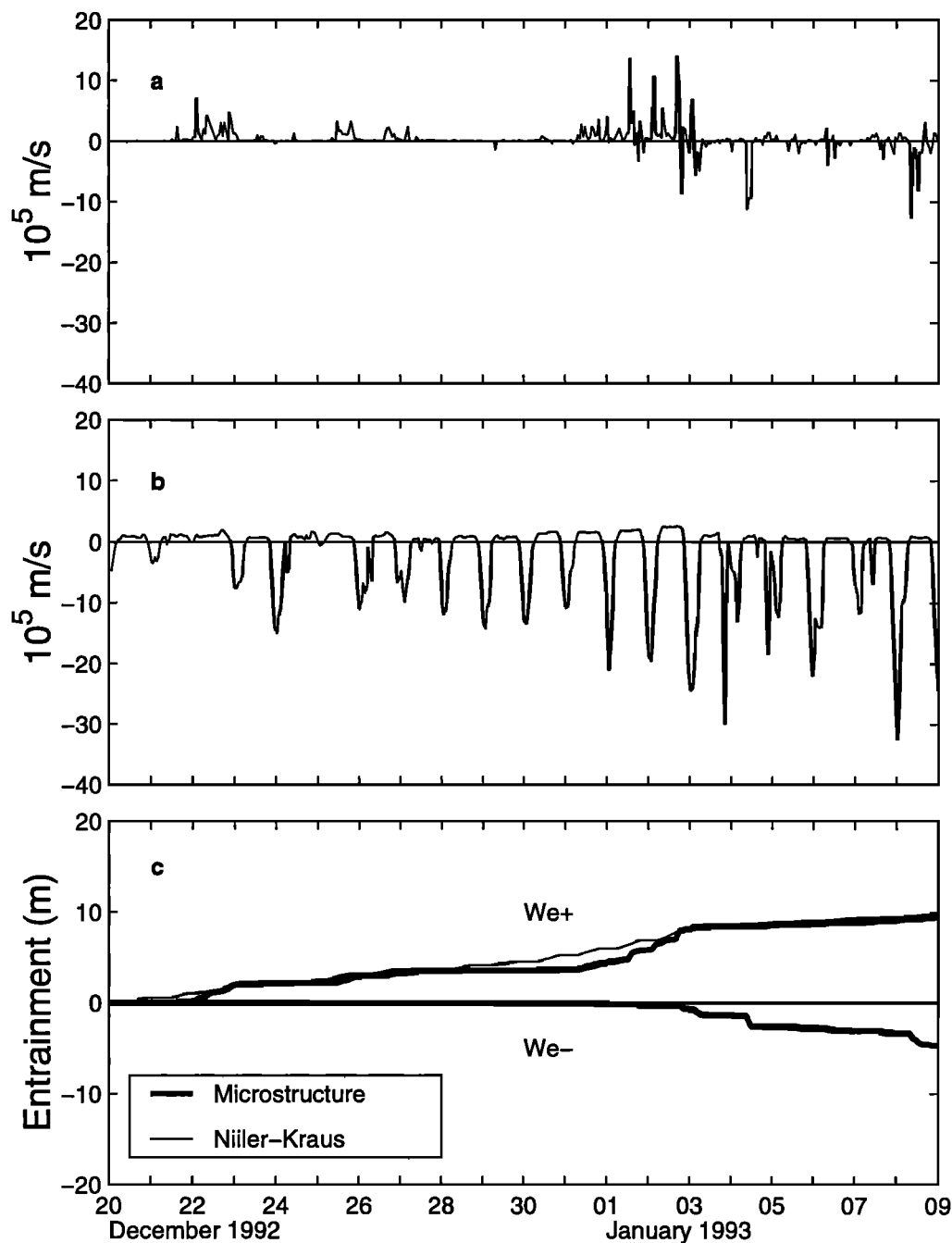
Figure 16. Diapycnal velocities across the $\sigma_\theta = 22$ isopycnal depth from the (a) microstructure data and (b) Niiler-Kraus formula and (c) their temporal cumulative effects. The velocities are separated into positive (w_e+) and negative (w_e-) parts in the cumulative calculations $(w_e-$ from Niiler-Kraus formula is not shown).

From the isopycnal boundary method, both diapycnal turbulent flux and diapycnal advection (vertical entrainment) are important to the surface layer heat and salt balances above the $\sigma_\theta = 22$ depth (Figures 17 and 18). The total heat flux across this isopycnal is more than 30 W m^{-2}. The WWB conditions typically prevail for about 2 months of a year [*Smyth et al.*, 1996b]. During the rest of the year, the total heat flux across $\sigma_\theta = 22$ is weak [*Wijesekera and Gregg*, 1996]. If we use 2 W m^{-2} to represent the rest of the year, which is the

upper limit of the heat flux at 100 m during the weak wind cruise 1 survey of the IOP [*Wijesekera and Gregg*, 1996], then we obtain an annual mean heat flux across the $\sigma_\theta = 22$ depth of 7 W m^{-2}. *McPhaden and Hayes* [1991] estimated a long-term mean heat flux of 5 W m^{-2} at 75 m in the warm pool region based on the entrainment flux only due to wind work; this is comparable with our estimate.

We have also analyzed the salt budget during the other two cruises of the R/V *Wecoma* survey. The anal-
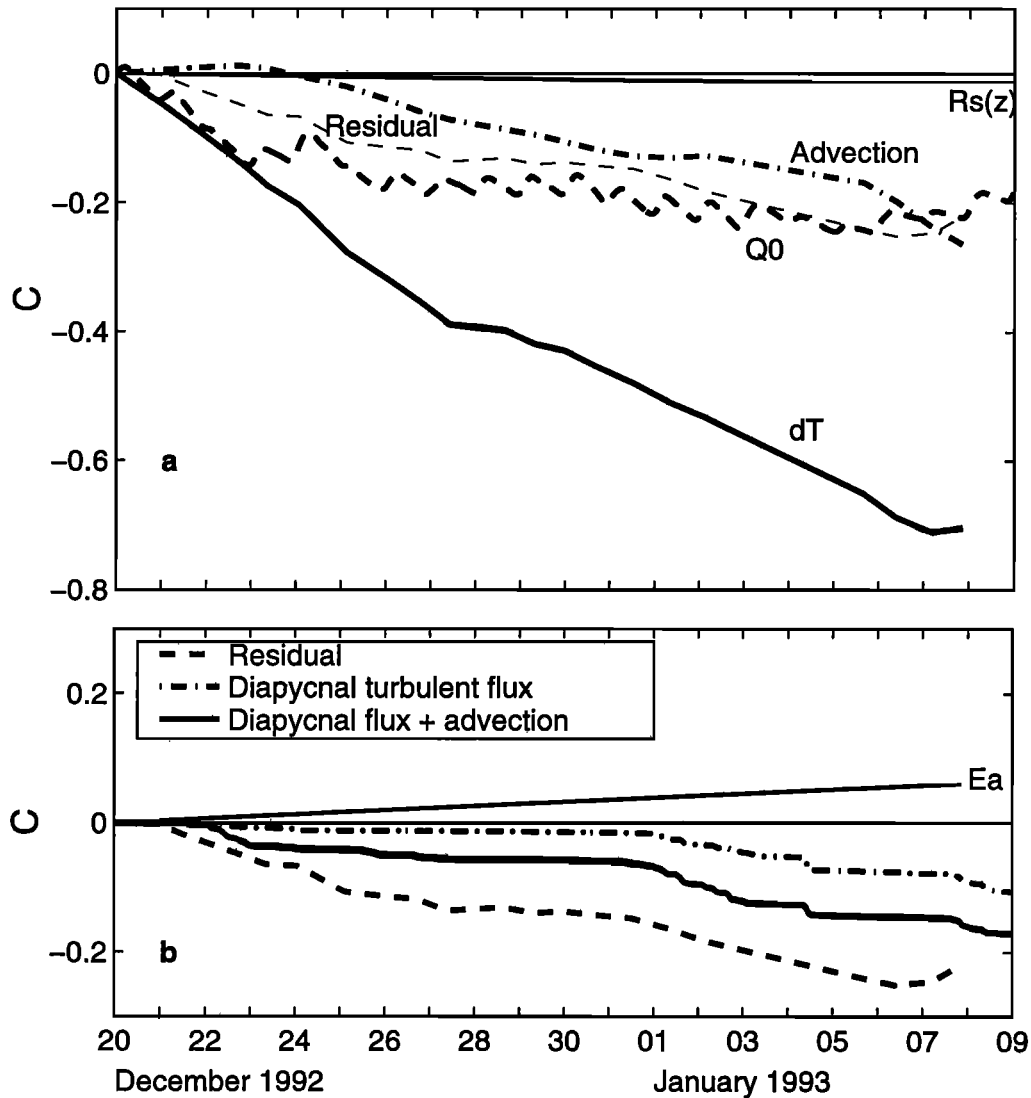
Figure 17. (a) Cumulative mean temperature change above the $\sigma_\theta = 22$ isopycnal depth. The advection term is the sum of mean advection and stratified shear flow advection. The diapycnal turbulent flux and diapycnal advection are part of the residual term. (b) Comparison of the residual with the diapycnal turbulent flux, the sum of diapycnal turbulent flux, and diapycnal advection across the isopycnal depth. E_a is the cumulative error in advection terms.

ysis of cruise 1 yields a mean rain rate of 2.2 mm d^{-1} during a 15-day time period (November 15–30, 1992), and the analysis of cruise 3 yields a mean rain rate of 4.6 mm d^{-1} during a 15-day time period (January 29 to February 12, 1993) [*Feng*, 1997; *Bradley and Weller*, 1997]. Averaging over the three cruises, a mean rain rate of 8 mm d^{-1} is obtained. Considering a mean evaporation rate of 3.8 mm d^{-1}, the net freshwater flux from our analysis is consistent with the annual mean estimation of *Donguy* [1987], 1.5 m y^{-1} (4.1 mm d^{-1}).

Because the layer above the $\sigma_\theta = 22$ depth is not an isothermal or isohaline layer, both positive and negative diapycnal velocities will affect the heat and salt balances in the surface layer, while negative advection (detrainment) is less efficient than positive advection (entrainment). Thus it is only a crude approximation

to simply assume that detrainment has no effect on the surface layer.

One other problem related to our budget estimation is that the vertical flux terms are all from point measurements. There is no problem for the surface heat flux, according to the intercomparison work by *Weller and Anderson* [1996]. However, the rain rate estimations still need further intercomparison [*Godfrey et al.*, 1998; *Bradley and Weller*, 1997]. Cruise average radar rain rate data show spatial variations over the survey domain of a factor of 4 [*Short et al.*, 1997]. Such variations must be taken into account when calculating upper ocean freshwater budgets. The ocean surface processes in response to the WWB have spatial scales comparable to the survey domain so that a point measurement might be insufficient to determine the mean vertical (diapyc-
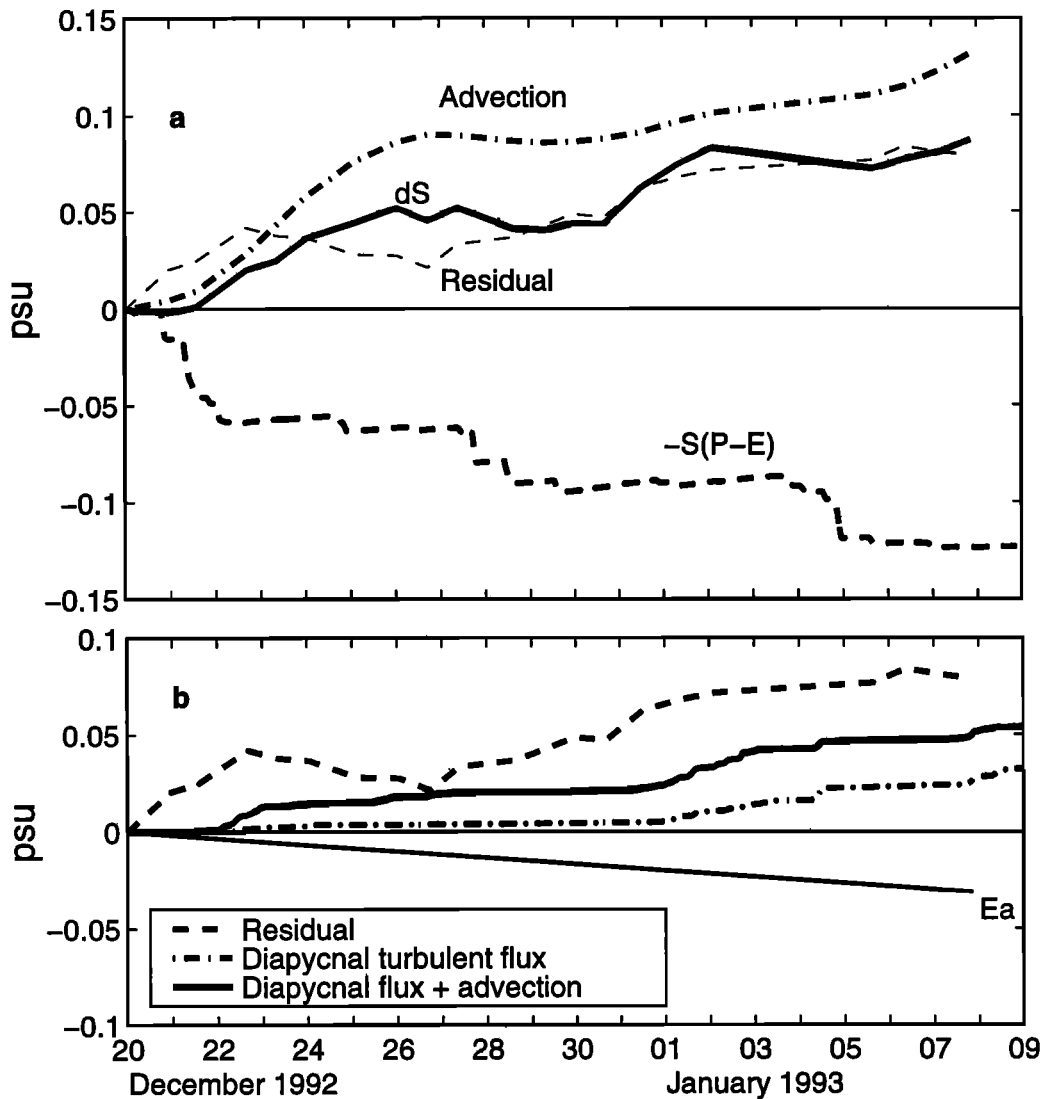
Figure 18. Same as Figure 17 but for salinity.

nal) turbulent flux and diapycnal advection over this region. Fortunately, the point measurements, the WHOI mooring, and R/V *Moana Wave*, are very close to the crossover point of the survey. Assuming linear spatial variations of the vertical processes, the point measurements should represent the mean over the whole region. The gradient Richardson number (Ri) at the isopycnal depth of $\sigma_\theta = 22$ does not have a significant meridional variation trend across the survey domain, whereas the meridional variation of Ri at 55 m seems to have a linear trend over the domain (Figure 19). The zonal variations of Ri are generally small.

6. Summary

In this paper, the R/V *Wecoma* IFA survey data are used to estimate the advection effects on the near surface layer heat and salt balances in response to a WWB. It turns out that the butterfly survey can resolve the

horizontal gradients of temperature and salinity on the timescale of 3 days with the repeated survey time of 1.5 days. This survey pattern resolves the main variations related to the December 1992 WWB at the center of the IFA region.

Two methods are used to analyze the heat and salt balances in the near surface layer. One uses a fixed thickness control volume from which the budgets can be computed directly using the temperature and salinity tendency equations; the other uses an isopycnal depth as the lower boundary of the control volume, in which case the mean temperature can be better related to the sea surface temperature and the low-mode internal wave effects can be effectively eliminated from the advection term calculation.

In both cases, the surface layer heat budget can be balanced within 10 W m^{-2} over a 19-day time period. The surface layer salinity can be balanced by reducing the R/V *Moana Wave* precipitation rate estimate
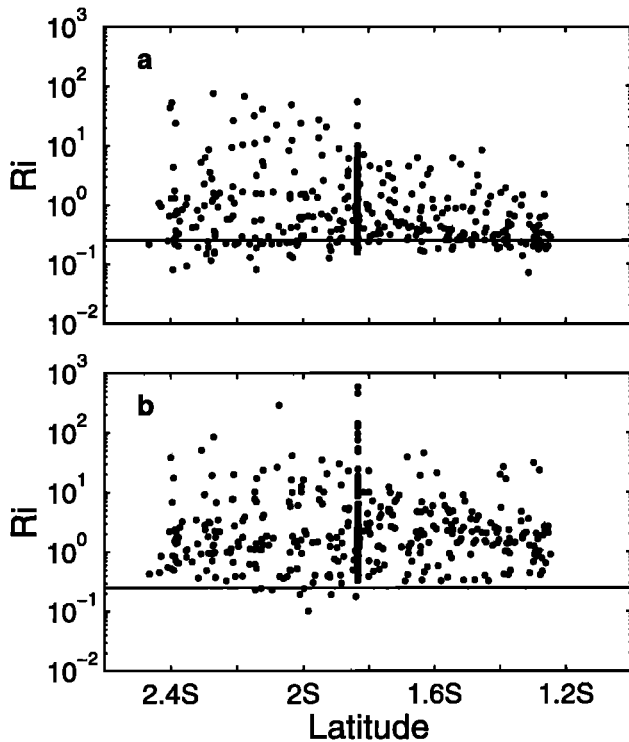
Figure 19. Gradient Richardson number (Ri) calculated from the R/V *Wecoma* density and velocity data as a function of latitude at (a) 55 m and (b) the depth of σ_θ=22 $\mathrm{kg\,m^{-3}}$ depth. The solid lines in the two plots are $Ri = 0.25$.

by 20%. In other words, we can predict the rain rate from the ocean budget to be 15.4 $\mathrm{mm\,d^{-1}}$ during this time period. This number is closer to the optical rain gauge measurements on the R/V *Wecoma* [*Bradley and Weller*, 1997]. Some of the difference may be due to the spatial variation of rain rate.

In both control volume methods, the advection terms are important in both the temperature and salinity balances, though they have different forms. Thus, even in the center of the warm pool region, the advection effects cannot be generally neglected in order to close the heat and salt budgets. The error in the heat advection estimation is 11 $\mathrm{W\,m^{-2}}$ over this 19-day time period, which is comparable with errors in other terms, such as the surface heat flux and the vertical turbulent flux.

In the isopycnal boundary method, the estimated diapycnal turbulent flux and diapycnal advection (entrainment) are almost equally important. The total heat flux across the $\sigma_\theta = 22$ surface is more than 30 $\mathrm{W\,m^{-2}}$ during this study time period.

Appendix A: Linear Fit

In order to obtain the best estimates of the spatial and temporal gradients from the R/V *Wecoma* survey data, the time interval used in each estimate includes two complete circuits of the butterfly pattern. The beginning and end of each time interval are the times when

the ship is near the crossover point to avoid misinterpreting the temporal and spatial gradients determined by the fitting. Each time interval has approximately 3 days, so that the contribution from variabilities on shorter timescales can not be fully resolved. Some intervals are excluded, such as near January 4 and after January 9, when the data only cover part of the region and would give a biased estimate of the gradients. The center of the time interval and the crossover point are used to represent the results. There are altogether 20 time intervals we select during cruise 2 of the R/V *Wecoma* survey, and the adjacent time intervals usually have overlapping time. Thus the 20 time intervals cover approximately 20 days. Note that in the cumulative calculation the integration is from December 20, 1992, to the central time of the last time interval, which is approximately 19 days.

In the temperature and salinity fits, the errors in the mean values are negligible. Thus, in the cumulative property analyses, the temporal gradients are not used. Instead, we use the mean values themselves, such as $\overline{T}$ and $\overline{S}$, in order to avoid the cumulative errors of the integrations of the temporal gradients. In this way, we can almost nullify the errors in these terms. The error estimations of the cumulative advection terms require a decorrelation timescale, where 3 days is used. This timescale is selected because this is the minimum timescale that the horizontal gradients can be resolved and is also the approximate timescale of the WWB peaks.

In the fixed depth heat balance, from the bootstrap analysis, the standard errors for the estimates of $\overline{u}(z)$, $\overline{v}(z)$ and $w(z)$ are $\Delta u(z)$, $\Delta v(z)$, and $\Delta w(z)$, and the errors for the temperature gradients are $\Delta T_x(z)$ and $\Delta T_y(z)$, then the errors for the three advection terms in the 3-day analysis are

$$\Delta \left[\int_{-h}^{0} u \frac{\partial T}{\partial x} dz \right] \leq \int_{-h}^{0} \left[\Delta u \left| \frac{\partial T}{\partial x} \right| + |u| \Delta T_x \right] dz = \delta_x,$$

$$\Delta \left[\int_{-h}^{0} v \frac{\partial T}{\partial y} dz \right] \leq \int_{-h}^{0} \left[\Delta v \left| \frac{\partial T}{\partial y} \right| + |v| \Delta T_y \right] dz = \delta_y,$$

$$\Delta \left[\int_{-h}^{0} w \frac{\partial T}{\partial z} dz \right] \leq \int_{-h}^{0} \Delta w \left| \frac{\partial T}{\partial z} \right| dz = \delta_z.$$

Note that the errors of $\partial T/\partial z$ are negligible compared to those of w. Assuming that δ_x, δ_y, and δ_z are independent, the error for the total advection in the 3-day analysis is

$$\Delta \left[\int_{-h}^{0} \left(u \frac{\partial T}{\partial x} + v \frac{\partial T}{\partial y} + w \frac{\partial T}{\partial z} \right) dz \right] \leq (\delta_x^2 + \delta_y^2 + \delta_z^2)^{\frac{1}{2}}.$$

The residual of heat balance (Figure 13) tends to have a decorrelation scale of nearly 2 days. Also, we do not consider the decorrelation scale in the vertical inte-

gration of error. Assuming that there are two degrees of freedom in the vertical and a 2-day decorrelation in time, we have overestimated the standard error in the advection terms by nearly a factor of 2.

In the isopycnal boundary method, we first calculate the mean values $T_a(x_0, y_0)$, $S_a(x_0, y_0)$, and $\mathbf{u}_a(x_0, y_0)$ by simply vertically integrating $T(x_0, y_0, z)$, $S(x_0, y_0, z)$, and $\mathbf{u}(x_0, y_0, z)$ from sea surface to the isopycnal depth at each hourly data point (x_0, y_0). Then we determine the deviations $T'(x_0, y_0, z)$, $S'(x_0, y_0, z)$, and $\mathbf{u}'(x_0, y_0, z)$ by subtracting the mean values from $T(x_0, y_0, z)$, $S(x_0, y_0, z)$, and $\mathbf{u}(x_0, y_0, z)$. Finally, we vertically integrate $T'\mathbf{u}'$ and $S'\mathbf{u}'$ from sea surface to the isopycnal depth at (x_0, y_0) to determine $\int_{-h}^{0} T'\mathbf{u}' dz$ and $\int_{-h}^{0} S'\mathbf{u}' dz$, which are also functions of (x_0, y_0). The horizontal gradients in the advection terms are calculated from the near 3-day linear fit of above terms. The bootstrap method is used to estimate their errors. It is assumed that the errors in the mean advection and stratified shear flow advection in (5) and (6) are independent.

Appendix B: Diapycnal Velocity

Here we discuss the equivalency of the two methods to calculate the diapycnal velocity: the density conservation method, (13), and the definition, (11). When assuming a linear relation between ρ, T and S, we can combine (1) and (2) yielding,

$$\frac{\partial \rho}{\partial t} + \mathbf{u} \cdot \nabla \rho + w \frac{\partial \rho}{\partial z} = \frac{\alpha}{\rho_0 C_P} \frac{\partial R_S}{\partial z} + \frac{\partial}{\partial z}\left(K_\rho \frac{\partial \rho}{\partial z}\right).$$

Equation (11) can be rewritted as

$$w_e \frac{\partial \rho}{\partial z} = \frac{\partial \rho}{\partial t} + \mathbf{u} \cdot \nabla \rho + w \frac{\partial \rho}{\partial z}$$

by replacing $\partial h/\partial t$ with $(\partial \rho/\partial t)/(\partial \rho/\partial z)$, etc. Combining the above two equations, (13) is obtained.

Now let us consider a simple case of the solar radiation flux to illustrate how the diapycnal velocity affects the mean properties in the surface layer (S. Godfrey, personal communication, 1997). In this case, there is no motion of any kind and no turbulence; the density is only determined from the temperature so that an isotherm can be used to represent an isopycnal. Figure B1a shows the radiation flux near an isotherm depth D, where the temperature equals T (Figure B1d). We assume that the flux $R_S(z)$ is linearly decreasing with depth, and the flux at depth D is F. Because this is a linear system, the radiation flux can be separated into two parts: one part has a constant flux of F (Figure B1b); the other part contains the linear trend with zero flux at depth D (Figure B1c). As an effect of the first part, there is no temperature change near depth D (Figure B1e), but the radiation flux is nonzero. This heat loss needs to be included in estimating the rate of change of depth-mean temperature above the
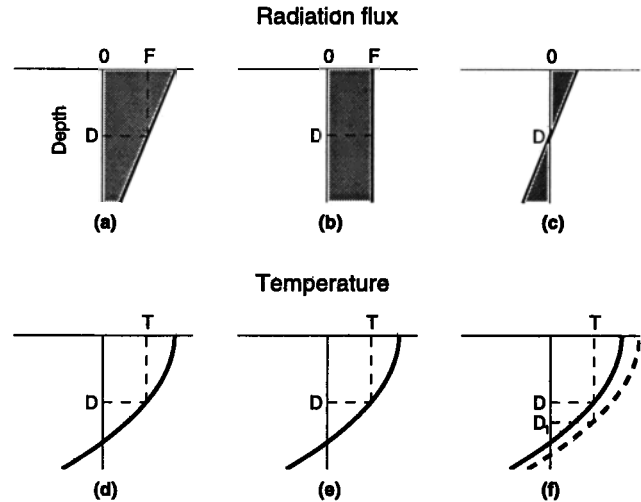
Figure B1. A sketch for the diapycnal velocity. (a) The radiation profile near depth D, which can be separated into (b) a mean part with a value of F and (c) a linear trend. (d) The original temperature profile near depth D. (e) The temperature change due to a mean part with a value of F. (f) The temperature change due to a linear tread. T is a selected isotherm, which deepens from D to D_1 in Figure B1f because of positive diapycnal velocity.

isotherm. Under the second part, the radiation flux at depth D is zero. However, the flux convergence causes the temperature to increase near D (Figure B1f). The isothermal surface at depth D would deepen at a speed $w = (\partial \rho/\partial t)/(\partial \rho/\partial z) = [(\alpha \partial R_S/\partial z)/(\rho_0 C_p)]/(\partial \rho/\partial z)$, because of absorption of solar radiation, so that we need to relocate the isotherm T, which is at depth D_1. We call this entrainment or diapycnal advection. In this process, water is in effect entrained at the original temperature of water between depths D and D_1, which is lower than the average temperature above depth D. The rate of increase of mean temperature above the depth of this isopycnal will be reduced by the entrainment process, as well as by direct heat loss out of the bottom. The same argument applies to the turbulent flux.

References

Anderson, S.P., R.A. Weller, and R. Lukas, Surface buoyancy forcing and the mixed layer of the western Pacific warm pool: Observations and 1-d model results, *J. Clim.*, *9*, 3056-3085, 1996.

Bradley, F., and R. Weller (Eds.), Fourth workshop of the TOGA COARE air-sea interaction (flux) working group, report, 72 pp., Woods Hole Oceanogr. Inst., Woods Hole, Mass., 1997.

Chen, S., R.A. Houze Jr., and B. Mapes, Multiscale variability of deep convection in relation to large-scale circulation in TOGA COARE, *J. Atmos. Sci.*, *53*, 1380-1409, 1996.

Cronin, M.F., and M.J. McPhaden, The upper ocean heat balance in the western equatorial Pacific warm pool during September-December 1992, *J. Geophys. Res.*, *102*, 8533-8553, 1997.

Donguy, J., Recent advances in the knowledge of the climatic variations in the tropical Pacific ocean, *Prog. Oceanogr.*, *19*, 49-85, 1987.

Efron, B., and R.J. Tibshirani, Bootstrap methods for standard errors, confidence intervals and other measures of statistical accuracy, *Stat, Sci.*, *1*, 54-77, 1986.

Eldin, G., T. Delcroix, C. Henin, K. Richards, Y. du Penhoat, J. Picaut, and P. Rual, Large-scale current and thermohaline structures along 156° E during the COARE Intensive Observation Period, *Geophys. Res. Lett.*, *21*, 2681-2684, 1994.

Fairall, C., E.F. Bradley, D.P. Rogers, J.B. Edson, and G.S. Young, The TOGA COARE bulk flux algorithm, *J. Geophys. Res.*, *101*, 3747-3764, 1996.

Feng, M., Semidiurnal tide and heat/salt balance in the western equatorial Pacific during TOGA COARE, Ph. D. thesis, 143 pp., Inst. of Oceanol., Chin. Acad. of Sci., Qing Dao, 1997.

Feng, M., M.A. Merrifield, R. Pinkel, P. Hacker and A.J. Pluddemann, E. Firing, R. Lukas and C. Eriksen, Semidiurnal tides observed in the western equatorial Pacific during Tropical Ocean-Global Atmosphere Coupled Ocean-Atmosphere Response Experiment, *J. Geophys. Res.*, in press, 1998.

Godfrey, J.S., and E. Lindstrom, The heat budget of the equatorial western Pacific surface mixed layer, *J. Geophys. Res.*, *94*, 8007-8017, 1989.

Godfrey, J.S., R.A. Houze Jr., R.H. Johnson, R. Lukas, J.-L. Redelsperger, A. Sumi, and R. Weller, Coupled Ocean-Atmosphere Response Experiment (COARE): An interim report, *J. Geophys. Res.*, in press, 1998.

Gregg, M.C., The coupled structures and fluxes in a deep convecting mixed layer, in *Dynamics of the Oceanic Surface Mixed Layer*, Aha Hulikoa Proceedings, Honolulu, HI, 1987, edited by P. Muller and D. Henderson, pp. 1-23, Univ. of Hawaii, Honolulu, 1987.

Harrison, D.E., and G.A. Vecchi, Westerly wind events in the tropical Pacific, 1986–1995, *J. Clim.*, *10* 3131-3156, 1997.

Huyer, A., P.M. Kosro, R. Lukas, and P. Hacker, Upper-ocean thermohaline fields near 2° S,156° E during TOGA-COARE, November 1992 to February 1993, *J. Geophys. Res.*, *102*, 12,749-12,784, 1997.

Lukas, R. and E. Lindstrom, The mixed layer of the western equatorial Pacific ocean, *J. Geophys. Res.*, *96*, suppl., 3343-3358, 1991.

McDougall, T.J., and Y. You, Implications of the nonlinear equation of state for upwelling in the ocean floor, *J. Geophys. Res.*, *95*, 13,263-13,276, 1990.

McPhaden, M.J., and S.P. Hayes, On the variability of winds, sea surface temperature, and surface layer heat content in the western equatorial Pacific, *J. Geophys. Res.*, *96*, 3331-3342, 1991.

Moum, J.N., The quest for K_ρ, *J. Phys. Oceanogr.*, *20*, 1980-1984, 1990.

Moum, J.N., M.C. Gregg, R.-C. Lien, and M.-E. Carr, Comparison of turbulent kinetic energy dissipation rates from two ocean microstructure profilers, *J. Atmos. Oceanic Technol.*, *12*, 346-366, 1995.

Niiler, P.P., and E.B. Kraus, One-dimensional models of the upper ocean, in *Modelling and Prediction of the Upper Layers of the Ocean*, edited by E.B. Kraus, pp. 143-172, Pergamon, Tarrytown, N. Y., 1977.

Osborn, T.R., Estimates of the local rate of vertical diffusion from dissipation measurements, *J. Phys. Oceanogr.*, *10*, 83-89, 1980.

Short, D.A., P.A. Kucera, B.S. Ferrier, J.C. Gerlach, S.A. Rutledge and O.W. Thiele, Shipboard radar rainfall patterns within the TOGA/COARE IFA, *Bull. Am. Meteorol. Soc.*, 78, 2817-2836, 1997.

Siegel, D.A., J.C. Ohlmann, L. Washburn, R.R. Bidigare, C.T. Nosse, E. Fields, and Y. Zhou, Solar radiation, phytoplankton pigments and the radiant heating of the equatorial Pacific warm pool, *J. Geophys. Res.*, *100*, 4885-4891, 1995.

Smyth, W.D., D. Hebert, and J.N. Moum, Local ocean response to a multiphase westerly windburst, 1, Dynamic response, *J. Geophys. Res.*, *101*, 22,495-22,512, 1996a.

Smyth, W.D., D. Hebert, and J.N. Moum, Local ocean response to a multiphase westerly windburst, 2, Thermal and freshwater responses, *J. Geophys. Res.*, *101*, 22,513-22,533, 1996b.

Sprintall, J., and M. Tomzak, Evidence of the barrier layer in the surface layer of the tropics, *J. Geophys. Res.*, *97*, 7305-7316, 1992.

Stevenson, J.W., and P.P. Niiler, Upper ocean heat budget during the Hawaii-to-Tahiti shuttle experiment, *J. Phys. Oceanogr.*, *13*, 1894-1907, 1983.

Webster, P.J., and R. Lukas, TOGA COARE: The coupled ocean-atmosphere response experiment, *Bull. Am. Meteorol. Soc.*, *73*, 1377-1415, 1992.

Weller, R.A., and S.P. Anderson, Surface meteorology and air-sea fluxes in the western equatorial Pacific warm pool during the TOGA Coupled Ocean-Atmosphere Response Experiment, *J. Clim.*, *9*, 1959-1990, 1996.

Wijesekera, H.W., and M.C. Gregg, Surface layer response to weak winds, westerly bursts, and rain squalls in the western Pacific warm pool, *J. Geophys. Res.*, *101*, 977-997, 1996.

M. Feng, P. Hacker, and R. Lukas, School of Ocean and Earth Science and Technology, University of Hawaii, Honolulu, HI 96822. (e-mail: mfeng@soest.hawaii.edu; hacker@soest.hawaii.edu; rlukas@soest.hawaii.edu;)